Gyrokinetic modelling of electron and boron density profiles of H–mode plasmas in ASDEX Upgrade

C. Angioni, R. M. McDermott, E. Fable, R. Fischer, T. Pütterich, F. Ryter, G. Tardini and the ASDEX Upgrade Team

Max-Planck-Institut für Plasmaphysik, EURATOM Association, D-85748 Garching, Germany

Abstract. Local gyrokinetic calculations of the logarithmic gradients at mid–radius of both electron and boron densities in ASDEX Upgrade H–mode plasmas are presented and compared to the experimental observations. The experimental results show that both the electron and the boron density profiles increase their peaking in response to the addition of central electron cyclotron heating over a background of neutral beam injection heating. The boron density profiles are always less peaked than the electron density profiles in the confinement region, and are flat or even slightly hollow in the presence of neutral beam injection heating only. The experimental behaviours are well reproduced by the theoretical predictions. The agreement allows the identification, through theoretical modelling, of the transport mechanisms responsible for the observed dependences. In particular, the observed increase of the logarithmic electron density gradient with increasing central electron heating is explained by a concurrent reduction of the outward pure convection and an increase of the inward thermodiffusion. In addition, it is found that the plasma toroidal rotation velocity and its radial gradient play a non–negligible role in the turbulent boron transport, and allow the prediction of a decrease of boron peaking with increasing rotation velocity, which is consistent with the experimental observations.

PACS numbers: 52.25.Fi, 52.55.Fa, 52.65.Tt

1. Introduction

The understanding of the behaviour of the electron density profiles in tokamak plasmas has significantly improved during the last decade [1]. An important aspect in this research, with relevance also for the prediction of the behaviour of a fusion reactor, is the effect of central electron heating on the density of electrons and impurities. This topic has received consideration since the first applications of electron cyclotron heating (ECH) [2, 3, 4] and has been the subject of intense research also in more recent years, regarding both electron [5, 6, 7, 8, 9, 10, 11, 12, 13, 14] and impurity [15, 16, 17, 18, 19] transport. In particular, it has recently been recognized that localized central electron heating does not produce an electron density flattening ("pump–out") in all conditions as previously assumed, but that there are regimes in which the application of localized electron heating can lead to an increase of the peaking of the electron density profile [7]. A recent review of the experimental observations obtained so far [1] allows us to conclude that central electron heating regularly leads to density flattening at low densities in L–mode plasmas, and in some cases also in plasmas at very high densities, in these conditions due to a reduced effect of the Ware pinch (e.g. [6]). In contrast, at intermediate densities, the density profile can remain almost unaffected or even increase its peaking in response to central electron heating [7, 10]. From the theoretical standpoint, these opposite behaviours can be explained by the reversal of the thermodiffusive contribution to the particle flux when the turbulent state of the plasma moves from a regime dominated by ion temperature gradient (ITG) modes to a regime dominated by trapped electron modes (TEM) [20, 21, 7]. So far, a qualitative consistency between the experimental observations and the theoretical predictions has been obtained when comparing the observed response of the electron density profile to central ECH and the predicted most unstable modes present in the plasma from microinstability analysis [7, 10, 8, 12]. However, a detailed quantitative comparison of the predicted peaking of the electron density profile with the experimental measurements for this kind of effect is still missing.

In addition, transport mechanisms analogous to those producing electron particle transport are also predicted to produce turbulent impurity transport. Therefore, a more complete validation of the theoretical paradigm can be obtained when the density profiles of both electron and impurities are considered at the same time. However, while electron transport is mainly produced by turbulent processes, the calculation of the transport of impurities has to include both turbulent and neoclassical components.

In this work, we have examined the response to central electron heating of a set of plasmas in the high confinement mode (H–mode) in ASDEX Upgrade (AUG), where a strong increase in the peaking of the electron density profile has been measured with increasing ECH power, over a background of neutral beam injection (NBI) heating. At the same time, measurements of the intrinsic boron density profile show that the peaking of the boron density also increases with increasing ECH power, while remaining significantly less peaked than the corresponding electron density profiles. Boron has been considered in this work since this is the dominant low charge intrinsic impurity in AUG

discharges after a boronization is performed and hence provides the most reliable signal for charge exchange recombination spectroscopy measurements (AUG operates with a tungsten coating of all plasma facing components [22]).

These experimental results are modelled by means of local linear and nonlinear gyrokinetic simulations. The predicted logarithmic gradients of the electron density profiles are identified by matching the predicted ratio of the particle flux to the heat flux to that obtained from the experimental transport analysis. The latter is evaluated by particle and power balance analyses with interpretative transport simulations. The predicted boron logarithmic density gradients are identified by the condition of boron particle flux equal to zero. The present dataset of observations is limited and presents strong correlations among various parameters, which prevents us from identifying the control parameters that govern the electron and boron density responses within an empirical approach. However, by theoretical modelling some indications are obtained of the roles of various plasma parameters. In particular, the roles of toroidal rotation and its gradient are specifically analyzed in the study of boron transport.

In the next section, the experimental observations are reviewed, giving particular emphasis to the parameters which are relevant as inputs for the gyrokinetic calculations. In the third section, the theoretical predictions for the local logarithmic electron density gradients are presented. In Section 4 the modelling of the local logarithmic gradients of boron density is presented and the different contributions to the boron transport are analyzed and compared to those of the electrons. Finally, Section 5 draws the conclusions of this work and outlines possible further studies.

2. Experimental observations

Gyrokinetic modelling is applied to a set of experimental measurements of electron and boron density profiles obtained in a sequence of AUG plasma discharges at 600 kA, with toroidal magnetic field 2.45 T, and a edge value of the safety factor $q_{95} = 6.6$. The line average density is around 5×10^{19} m^{-3}. In these discharges, in addition to a background of auxiliary heating with neutral beam injection (NBI) at powers of 2.5 MW or 5 MW, central ECH powers from 0.6 MW to 2.2 MW are also applied, in phases 1 second long. These experiments were designed specifically to study the response of the core plasma toroidal rotation to localized electron heating, by varying electron heating powers and locations, from central to more peripheral. A complete description of the experimental set–up and of the experimental results, and a related transport analysis, particularly dedicated to the toroidal momentum transport, can be found in companion papers [23, 24]. In the present work, instead, the focus is on the density profiles and on the analysis and modelling of particle transport. Therefore, the problem of momentum transport is not considered directly here, nor that of heat transport. Modifications in the toroidal rotation profile, as well as modifications in other plasma parameters such as electron and ion temperatures, induced by the application of central electron heating, are taken into account in the analysis and the modelling of particle transport.

For the purposes of the present study, a dataset of 22 observations has been built,

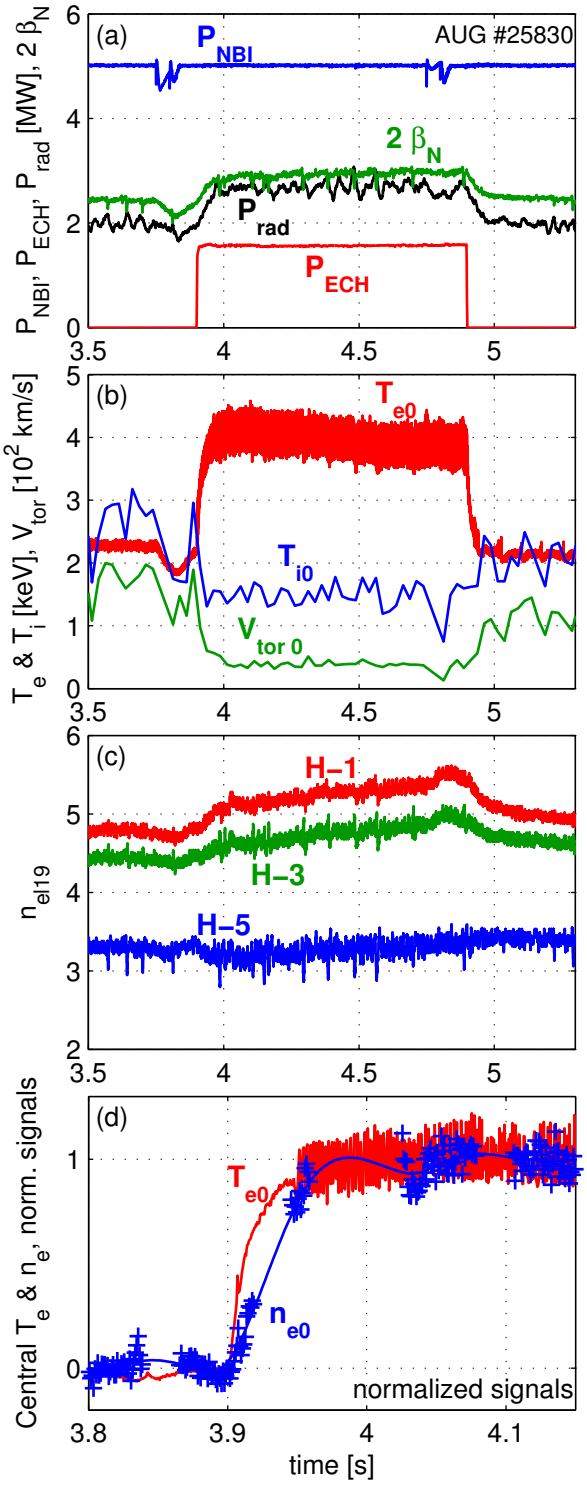

Figure 1. (a) Time traces of the NBI, ECH and radiated power, as well as the normalized pressure parameter β_N; (b) time traces of the central electron temperature, ion (boron) temperature and boron toroidal rotation velocity; (c) time traces of the central (H1), intermediate (H3) and peripheral (H5) chords of the DCN interferometer; and (d) time traces of the normalized signals of the central electron temperature and electron density, during a high power central ECH phase. Note the time window of (d) is different from the time windows of (a–c).

and has been then directly applied to produce the input for the gyrokinetic simulations. The observations in the dataset are obtained by taking time averages of the plasma kinetic profiles over time windows of 250 ms during the different heating phases. An example of such a heating phase, in which almost 2 MW of localized ECH are applied at $r/a = 0.05$ in addition to a background of 5 MW of NBI heating, is presented in figure 1, where time traces of a set of relevant parameters are plotted. In figure 1(a) the heating and radiated powers, as well as the time evolution of $\beta_N = \beta/(I_p/(aB_T)$ are shown. In figure 1(b), we observe that, as a consequence of the application of central electron heating, the central electron temperature increases strongly, while the central ion temperature and boron rotation decrease significantly. The central electron density increases also, as shown in figure 1(c), as indicated by the increase of the signal from the central chord (H–1) of the interferometer, while the signal from the most peripheral chord H–5 remains almost unchanged. Finally, in figure 1(d), time traces of the central electron temperature T_{e0} and central electron density n_{e0} are shown, normalized to 0 and 1 in the beam heated only phase and the ECH phase respectively, in a time window encompassing the ECH switch on. Specifically, the normalized signals plotted in figure 1(d) are obtained by computing $(T_{e0} - < T_{e0} >_{[3.8\ 3.9]})/(< T_{e0} >_{[4.0\ 4.1]} - < T_{e0} >_{[3.8\ 3.9]})$ and $(n_{e0} - < n_{e0} >_{[3.8\ 3.9]})/(< n_{e0} >_{[4.0\ 4.1]} - < n_{e0} >_{[3.8\ 3.9]})$, where the $< >_{[t_1\ t_2]}$ is the time average in the time interval $[t_1\ t_2]$. The electron density profiles, from which the central value is taken, are obtained by combining the integrated signals of the DCN interferometer with an edge lithium beam diagnostic by means of an integrated data analysis (IDA) method [25]. In figure 1(d), the small time windows in which density data are missing are a consequence of not sufficiently reliable lithium beam measurements, which prevented the IDA analysis in these phases. Still, it is evident from this figure that the characteristic time of the increase of the central electron temperature is much smaller than that of the electron density, suggesting that the increase of the central temperature can be the cause of the increase of the central density. Therefore, while the increase of the electron temperature is a direct consequence of the applied central electron heating, the increase of the central density can be considered as a transport effect, caused by the direct modification of other plasma parameters, such as the electron to ion temperature ratio and the plasma collisionality. The consequences of the application of 2 MW of central electron heating on the plasma profiles are shown in figure 2. Figures 2(a) and 2(b) show the increase of the peaking of the electron density and of the boron density profiles. The electron density profiles are reconstructed with the IDA method [25], while the boron measurements are obtained by change exchange recombination spectroscopy. The region of maximum logarithmic electron density gradient occurs between r/a = 0.4 and r/a = 0.6, which suggests that the local gyrokinetic modelling should be performed around r/a = 0.5. This is also the region of the plasma core in which the boron density profile measurements are most reliable. In addition, the central region of the plasma is affected by magnetohydrodynamical instabilities, mainly sawteeth [23, 24], which partly hamper the transport analysis. These are the main reasons for which the present analysis focuses on the behaviour of the plasma between $r/a = 0.4$ and $r/a = 0.6$. We observe that around mid–radius the boron density profile is flat and can be even slightly

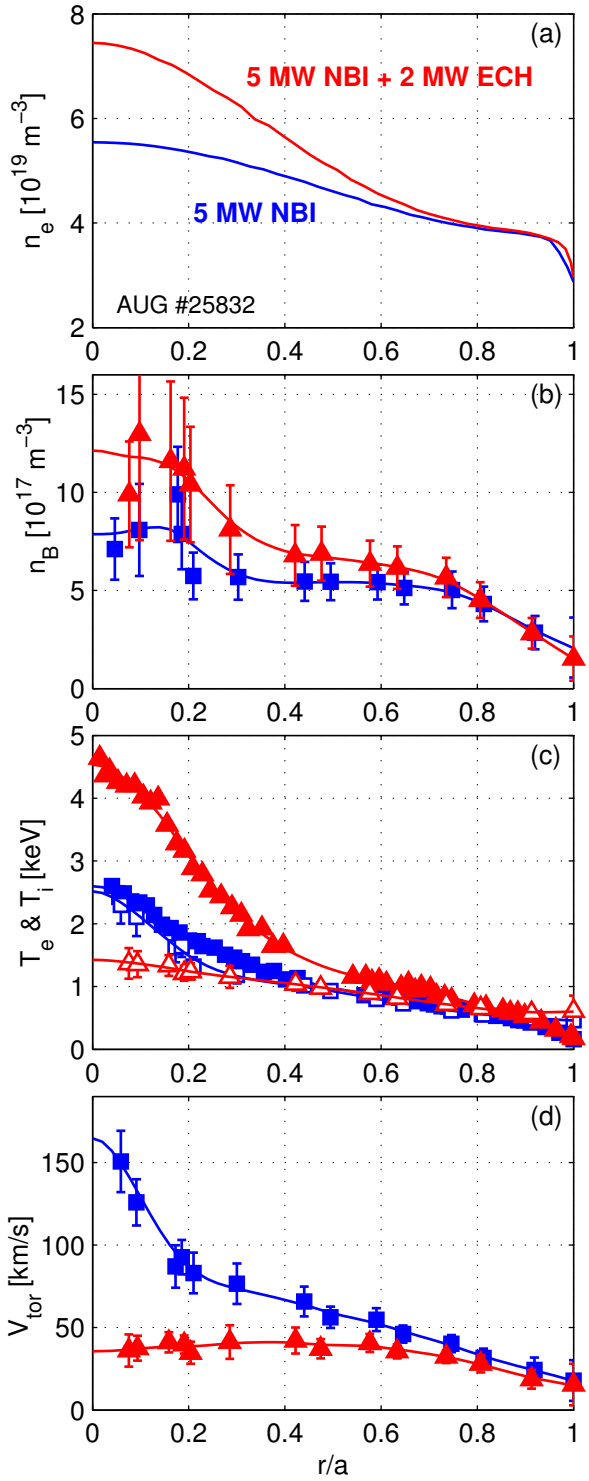

Figure 2. Plasma profiles comparing conditions with additional high central ECH (triangles pointing up) to those with NBI heating only (squares). (a) Electron density profiles (from IDA); (b) boron density profiles (from charge exchange recombination spectroscopy); (c) electron temperature (full symbols, from electron cyclotron emission radiometry) and ion temperature (open symbols, from charge exchange recombination spectroscopy); and (d) boron toroidal rotation velocity (from charge exchange recombination spectroscopy). In figures (b-d), solid lines show the cubic spline fits which have been used to compute the gradients and build the input of the gyrokinetic calculations.

hollow during the NBI only phase. In contrast, it becomes moderately peaked during the ECH phase. In figure 2(c) the electron temperature (full symbols) and the ion temperature profiles (open symbols) are plotted. During the NBI only phase, the two temperature profiles are close, while a strong separation of the two profiles is produced by the application of ECH, with an increased peaking of the electron temperature and a flattening of the ion temperature. The same takes place for the boron toroidal rotation profile, which is centrally peaked in the NBI only phase, and is strongly flattened by the additional application of central electron heating, as demonstrated in figure 2(d). The lines in these plots show the regularized fits obtained by cubic splines with tension on the raw data. These curves are directly applied in the power balance transport analysis, as well as to compute the local gradients, which are given as inputs to the gyrokinetic calculations.

By making averages of the regularized profiles over a radial window between r/a = 0.4 and r/a = 0.6, values of theoretically relevant parameters like the local logarithmic gradients, the ion to electron temperature ratio, and the electron collision frequency can be computed. The minor radius r, which is used in these plots and in the calculation of the gradients, is defined as the half width of the magnetic flux surface at the magnetic midplane, as required by the input of the gyrokinetic codes. In figures 3 and 4 a set of interesting scatter plots is presented, in which the local normalized logarithmic electron density gradient $R/L_{ne} = -(R/n_e)dn_e/dr$ and the local normalized logarithmic boron density gradient $R/L_{nB} = -(R/n_B)dn_B/dr$ are plotted as a function of various plasma parameters.

In figure 3(a,b), we observe that R/L_{ne} increases with increasing electron to ion temperature ratio, and decreases with increasing collisionality. Conditions with large T_e/T_i and low collisionality correspond also to conditions with large $R/L_{Te} = -(R/T_e)dT_e/dr$, figure 3(c), and relatively smaller $R/L_{Ti} = -(R/T_i)dT_i/dr$, figure 3(d). This implies that R/L_{ne} increases also with increasing L_{Ti}/L_{Te}. The present set of experimental results confirms, and extends to a significantly wider parameter domain, results obtained in previous studies in AUG. In particular, the increase of electron density peaking with ECH at intermediate densities in H–mode as well as at intermediate densities in L–mode plasmas was already noted to occur in [7, 10]. As already underlined in these previous works, the present experimental results further demonstrate that the often observed electron density flattening, dubbed "density pump–out", produced by central ECH is not a general phenomenon, and there are plasma conditions in which an opposite response to central ECH can be observed. Also the decrease of R/L_{Ti} and of the rotation in response to central ECH is consistent with previous observations [26, 27].

The corresponding values of the logarithmic boron density gradients are plotted in figure 4. We observe that around mid–radius R/L_{nB} is always significantly smaller than R/L_{ne}, figure 4(a). In the radial region around r/a = 0.5, the boron density profile is flat or even hollow in the presence of NBI only heating. These observations for a relatively light impurity like boron appear to be rather generic in typical NBI heated H–mode plasmas. They are consistent with observations of carbon density profiles obtained in other devices, like JET [28, 29]. It is only in the presence of strong ECH that boron

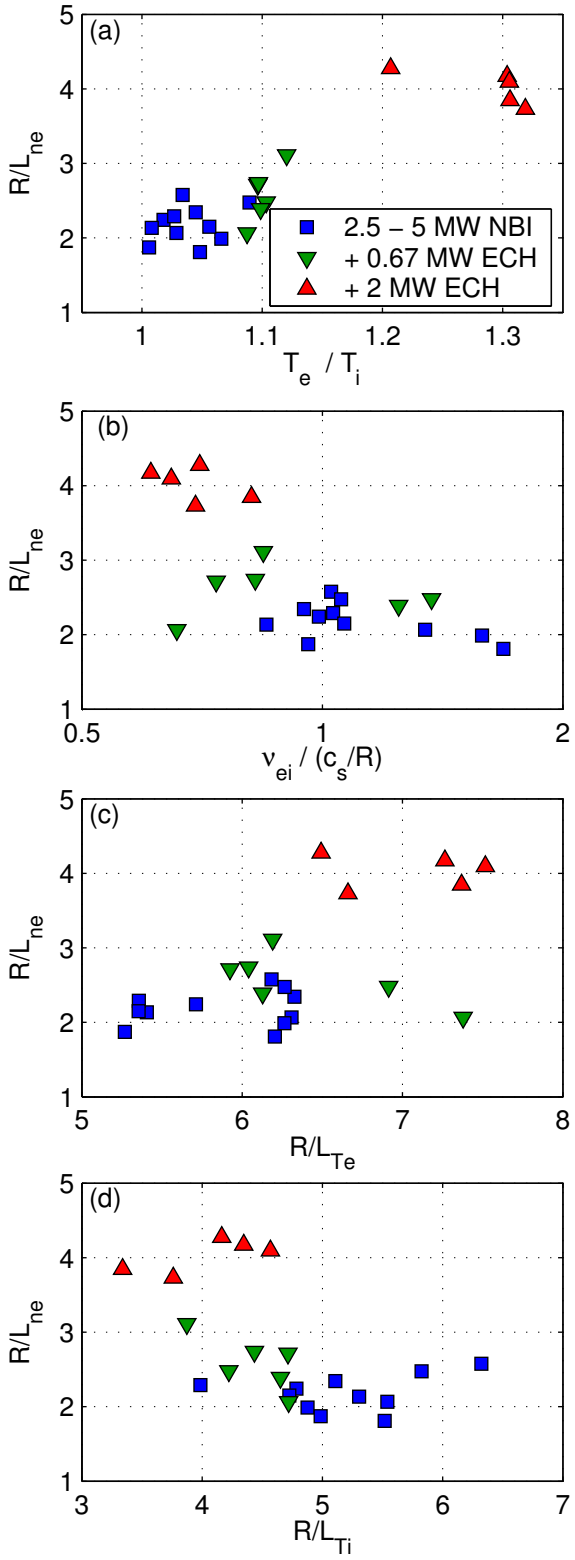

Figure 3. Scatter plots of the normalized logarithmic electron density gradient R/L_{ne} as a function of various plasma parameters: (a) the electron to ion temperature ratio T_e/T_i; (b) the normalized electron collision frequency $\nu_{ei}/(c_s/R)$; (c) the normalized logarithmic electron temperature gradient; and (d) the normalized logarithmic ion temperature gradient. Different symbols indicate different heating phases, with NBI heating only (squares), with NBI and low central ECH (triangles pointing down) and with NBI and high central ECH (triangles pointing up).

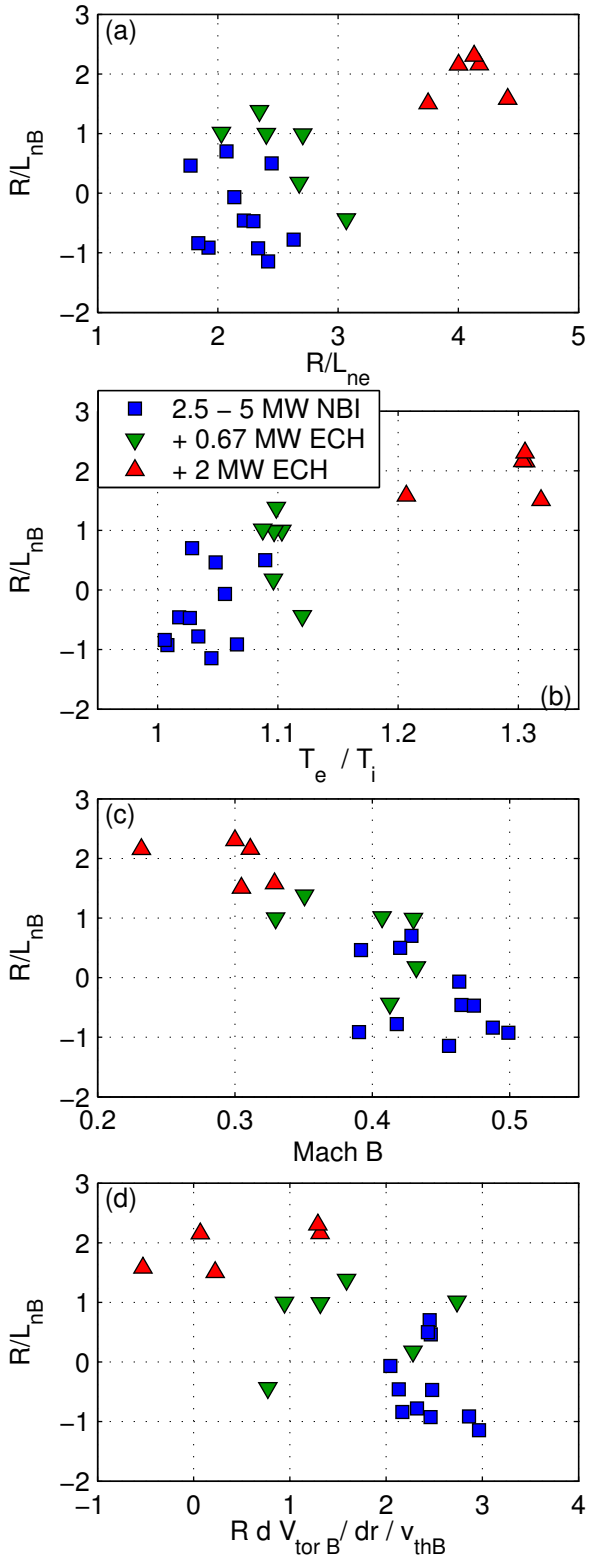

Figure 4. Scatter plots of the normalized logarithmic boron density gradient R/L_{nB} as a function of various plasma parameters: (a) the normalized logarithmic electron density gradient R/L_{ne}; (b) the electron to ion temperature ratio T_e/T_i, (c) the boron Mach number $v_{tor\,B}/v_{th\,B}$; and (d) the normalized radial gradient of the boron toroidal velocity $(R/v_{th\,B})dv_{tor\,B}/dr$. Different symbols indicate different heating phases, with NBI heating only (squares), with NBI and low central ECH (triangles pointing down) and with NBI and high central ECH (triangles pointing up).

density profiles show a clear peaking around mid–radius, with values of $R/L_{nB} > 1$. Figures 4(b-d) show scatter plots of R/L_{nB} versus the electron to ion temperature ratio as well as with dimensionless local toroidal rotation parameters, that is the boron Mach number $M_B = v_{torB}/v_{thB}$, where $v_{thB} = \sqrt{2T_B/m_B}$ is the boron thermal velocity, and the normalized toroidal velocity gradient $u'_B = (R/v_{thB})dv_{torB}/dr$. We observe that slightly hollow or flat density profiles are obtained not only at low values of T_e/T_i, but also at high boron rotation M_B and large boron rotation gradient u'_B. In contrast, the largest values of R/L_{nB} are obtained not only at the largest values of T_e/T_i, but also at low values of u'_B and at the lowest values of M_B.

As the transport analyses presented in this work rely heavily on the calculation of the radial gradients of the measured plasma profiles it is important to be aware of the uncertainties in these parameters. Therefore, the uncertainties in the gradients have been estimated carefully following two procedures. The first makes use of the cubic spline fitting function, which has been used to produce the regularized profiles. For this procedure 10,000 cubic spline fits to the data were produced, where for each the measured data points were randomly displaced in the vertical direction according to a normal distribution centered on the actual measured value and with a standard deviation given by the experimental error bar. The radial gradient over the interval of interest ($0.4 \leq r/a \leq 0.6$) was then computed for all of the cubic spline fits, resulting in a normal distribution of radial gradients. The mean of this distribution represents the actual radial gradient at this location and the uncertainty on the gradient is given by the standard deviation of the distribution. The second procedure is similar, but instead of using the cubic spline fitting function, the local gradients are computer directly by linear interpolation on the raw data points over the radial interval of interest ($0.4 \leq r/a \leq 0.6$). We have found that the two approaches provide error bars for the local gradients which are very close, and which can be quantified in an absolute sense as an interval in the normalized gradients. These turn out to be $\Delta(R/L_{Te}) \simeq 0.5$, $\Delta(R/L_{Ti}) \simeq 1.3$, $\Delta(R/L_{nB}) \simeq 2.5$, and $\Delta((R/v_{th\,B})dv_{tor\,B}/dr) = 0.8$. For the electron density profiles, the uncertainty of the gradients has to be computed through the IDA reconstruction method, and can be estimated as $\Delta(R/L_{ne}) = 1.0$. We note in particular that the larger error bars in the local boron logarithmic density gradients reflect also the fact that the boron density profiles are flatter.

Of course, large correlations between several parameters are present in this small dataset, and within an empirical approach it is practically impossible to unambiguously identify the control parameters that govern the behaviour of the electron and the boron density profiles. It is, however, within such a context that theoretical modelling can become particularly useful. In the event that a satisfactory qualitative or even quantitative agreement is obtained between theoretical predictions and experimental observations, this not only contributes to the validation of the theoretical paradigm, but also provides a way towards the identification of the control parameters and the physical mechanisms governing the observed behaviour of the density profiles. The indications obtained by the theoretical modelling can be tested later with additional, dedicated, experimental investigations.

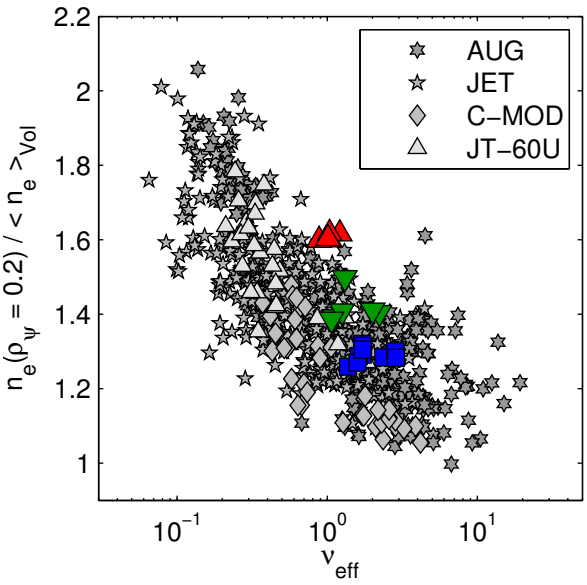

Figure 5. Density peaking, defined by the ratio of the density at $\rho_\Psi = 0.2$ (ρ poloidal) to the volume average density as a function of the effective collisionality, defined as $\nu_{\rm eff} = 0.1 Z_{\rm eff} \langle n_e \rangle R / \langle T_e \rangle^2$, where $\langle n_e \rangle$ and $\langle T_e \rangle$ are volume averaged electron density and electron temperature in 10^{19} m^{-3} and keV respectively. The AUG plasmas considered in this work are denoted by the larger symbols (squares for NBI heating only phases, triangles pointing down for NBI heating with additional low central ECH, and triangles pointing up for NBI heating with additional high central ECH). The data points from the previous multi–device database are plotted with smaller lighter symbols, and observations from the different devices are denoted with different symbols, as explained in the legend.

Before moving on to the modelling part of this paper, it is of interest to compare present experimental results with a set of previous results available in the literature. First of all, the density peaking obtained in the present discharges is plotted over the density peaking coming from a large database of observations [1], in which previous results from AUG [30], JET [28, 31], C–Mod [32] and JT–60U [33] have been combined. The scatter plot is presented in figure 5, where the same definitions used in [34] are applied. We observe that while the new data remain mostly within the scatter of the previous data, they show a dependence on collisionality which is stronger than the one obtained on average over the large database. The same conclusions are reached by comparing the local values of R/L_{ne} obtained in the present discharges with the scaling laws for R/L_{ne} at mid–radius built over databases of JET observations only [31, 35]. These considerations suggest that additional parameters other than the collisionality alone are affecting the peaking of the density profile in these more recent AUG discharges, in which T_e/T_i and L_{Ti}/L_{Te} can exceed unity by much more than they do on average in the database of previous observations.

More specifically, it is of interest to observe how the present results explore a parameter domain which is almost complementary with respect to that explored in previous AUG studies devoted to the effects of ECH in NBI heated H–modes [26, 27].

Despite the fact that the plasmas considered in those previous works were heated with the same amount of NBI and ECH power as those analyzed here, the modifications to the plasma profiles produced by the application of ECH and the consequent range of plasma parameters explored turns out to be significantly larger in the present study. From our present understanding, the main reason for this is connected to the different plasma currents at which the present experiments and the previous ones were carried out. In the present experiments, a low current of 600 kA is chosen to limit perturbations from sawtooth activity to the innermost region of the plasma, thereby reducing their impact on the transport analysis. The previous discharges [26] were performed instead at 1 MA, at approximatively the same magnetic field as the present discharges, with the goal of exploring low density H–mode regimes with high confinement and high performance. In the present discharges, the electron and ion temperatures are close in the NBI only phase, while the electron temperature exceeds significantly the ion temperature in the high ECH power phases. In contrast, in the previous experiments, the ion temperature exceeded the electron temperature in the NBI only heated phases, and the two temperature profiles became close to each other in the high ECH power phases, mainly due to the drop of the ion temperature [26, 27]. The plasmas considered in those previous works not only had a different safety factor profile, but also, and perhaps even more importantly, a higher total stored energy, and particularly a much higher pedestal top pressure. This is mainly a consequence of the higher plasma current, but also of a better H–mode confinement. The latter can be characterized through the so–called H_{IPB98} factor, which, during the high ECH phases, was around 1.1 in the previous discharges at 1 MA, and it is only 0.8 during the same heating phases in the present discharges at 600 kA (H_{IPB98} is the ratio of the experimental confinement time to the confinement time predicted by the scaling law IPB98(y,2) [36]). The better confinement of the previous high current discharges allowed the achievement of much higher plasma temperatures, despite rather similar plasma densities, at the same auxiliary heating powers. A one to one comparison shows that in present experiments in the presence of 5 MW of NBI and 2 MW of ECH, at a local density of 5×10^{19} m^{-3} at r/a = 0.5, the local electron temperature is only 1.3 keV, whereas in previous experiments at 1 MA, at a slightly lower local density of 4.3×10^{19} m^{-3}, electron temperatures of 4.0 keV were achieved, reaching much larger values of β_e, much lower values of collisionality, but also much larger values of the gyro–Bohm conductivity. This means that in the confinement region, around mid–radius, the present experiments have normalized heat fluxes that are much larger than the previous ones (we note that the gyro–Bohm normalization of the heat flux is proportional to $n_e T_e^{5/2}$ and is more than one order of magnitude larger for previous experiments as compared to present ones). In our present understanding, this is one of the main reasons why in the present 600 kA H–modes very large variations of the plasma profiles, and particularly of the electron temperature, are observed in response to the application of central ECH, reaching large values of T_e/T_i and of R/L_{Te} at mid–radius, close to those more regularly obtained in L–modes, which were not achieved in the previous H–mode experiments at much higher current.

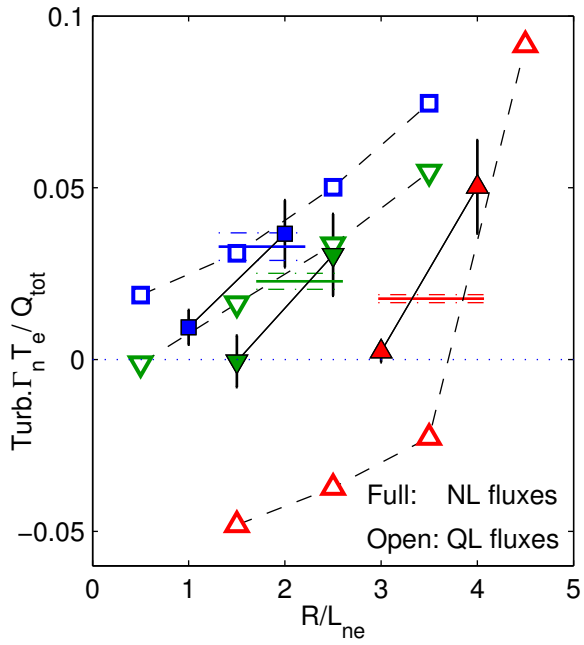

Figure 6. Ratio of the turbulent particle flux to the total turbulent heat flux obtained in quasi–linear GS2 (open symbols, dashed lines) and nonlinear GYRO (full symbols, solid lines) calculations, for three representative cases of the three heating phases, with NBI heating only (squares), NBI heating and low central ECH (triangles pointing down), NBI heating and high central ECH (triangles pointing up). The intersecting horizontal lines provide the corresponding experimental values deduced by particle and power balance analyses, and which include the neoclassical contributions of ion heat and particle Ware pinch fluxes, as given in Eq. (1). Upper and lower horizontal dash–dotted lines show the uncertainty on this parameter, taking into account a 50% error bar in the local heat flux profile of the radiated power.

3. Modelling of R/L_{ne}

The gyrokinetic modelling of the local value of R/L_{ne} has been performed with both linear and nonlinear calculations. For practical reasons, the linear calculations have been performed with the GS2 code [37, 38], while the nonlinear simulations have been performed with GYRO [39, 40]. The two codes have regularly been found to be in very good agreement (e.g. [41, 42]). The concurrent use of linear and nonlinear simulations is of interest since linear calculations are much less consuming in terms of computer time and allow investigations on wider parameter ranges. In addition, the validation of models for the quasi–linear fluxes against nonlinear simulations is important for the application of quasi–linear transport models in transport codes.

The modelling approach looks for the identification of the value of R/L_{ne} from the gyrokinetic simulations which matches the ratio between the particle flux and the total heat flux obtained from the experiment by particle and power balance analyses. To this purpose, the gyrokinetic calculations are performed by scanning the value of R/L_{ne}, while keeping all the other input parameters fixed at their experimental values. In the gyrokinetic calculations a Miller description [43] has been applied, which is appropriate

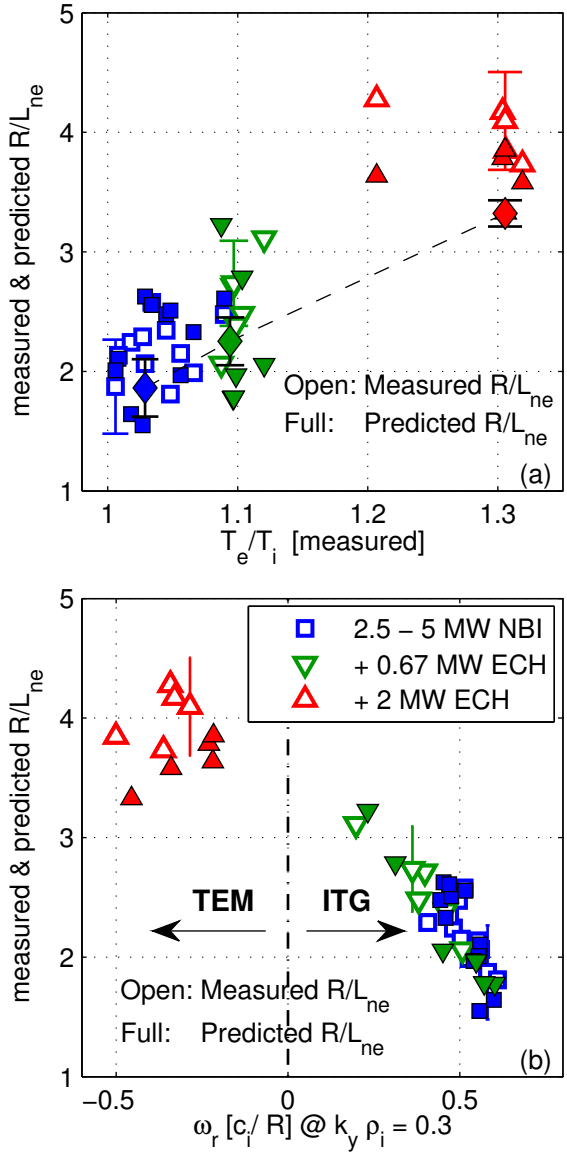

Figure 7. (a) Comparison between predicted (full symbols, quasi–linear GS2 with squares, triangles pointing down and triangles pointing up, nonlinear GYRO with diamonds connected by a dashed line) and measured (open symbols) values of R/L_{ne}, plotted as a function of the electron to ion temperature ratio T_e/T_i; and (b) same comparison, this time only for quasi–linear GS2 results, plotted as a function of the real frequency of the most unstable mode at $k_y\rho_i = 0.3$, for the entire dataset, with NBI heating only (squares), NBI heating and low central ECH (triangles pointing down), NBI heating and high central ECH (triangles pointing up).

for applications around mid–radius where the up–down asymmetry of the plasma is already weak. Magnetic equilibrium parameters have been extracted from equilibrium reconstructions obtained within full interpretative runs of TRANSP [44]. With linear simulations, 22 specific scans in R/L_{ne} have been performed for all the 22 observations of the experimental database, while with nonlinear simulations only three scans in R/L_{ne} have been performed, where each scan was dedicated to a single representative case for each of the three different heating phases.

The linear gyrokinetic simulations have been performed over a logarithmic binormal wave number spectrum of 10 values, from $k_y\rho_i = 0.12$ to $k_y\rho_i = 1.2$, and spectral averages have been performed assuming a dependence of the amplitude of the electrostatic potential fluctuations $|\phi_k|^2$ on the wave number k_y as proposed in [45]. The local flux–tube nonlinear simulations have been performed over 64 toroidal modes, up to $k_y\rho_s = 2.66$, in a box $L_x \times L_y = 90\rho_s \times 150\rho_s$, with 216 radial grid points and 256 grid points in the velocity space ($\rho_s = \sqrt{T_e m_i}/B$ and $\rho_i = \rho_s \sqrt{T_i/T_e}$). Pitch–angle scattering collisions are included in both linear and nonlinear calculations, and the experimental effective charge number $Z_{\rm eff} = 1.5$ has been included in the electron collision frequency.

The ratio of the particle flux to the total heat flux obtained in linear and nonlinear simulations is compared to the actual value achieved in the experiment. The latter is evaluated by considering that only the turbulent part of the fluxes are computed by the gyrokinetic calculations and assuming that only the particle fuelling due to NBI contributes non–negligibly to the particle flux at mid–radius [46]. Then the equation which is solved is the following,

$$\frac{\Gamma_{n\,\rm trb}}{Q_{\rm tot\,trb}} = \frac{\Gamma_{\rm NBI} - \Gamma_{\rm Ware}}{Q_{H\rm exp} - Q_{i\rm NC}}. \qquad (1)$$

Here, $\Gamma_{n\,\rm trb}$ and $Q_{\rm tot\,trb}$ are, respectively, the turbulent particle and total heat fluxes computed by the gyrokinetic simulations, $\Gamma_{\rm NBI} = \int dV S_{NBI}$ is the integral of the particle source density deposited by the beams up to r/a = 0.5, and analogously $Q_{H\rm exp} = \int dV P_{H\rm tot}$ is the volume integral of the total heating power density, $P_{H\rm tot} = P_{NBI} + P_{ECH} + P_{OH} - P_{\rm rad}$. The NBI particle source and heating power densities have been calculated with TRANSP and the ECH power density with the beam tracing code TORBEAM [47]. The largest uncertainty in this calculation is in the actual power density profile of the radiated power, which is rather significant in these shots, as shown in figure 1(a). This is not measured and has been calculated assuming a typical composition for the impurity content of these plasmas, with small concentrations of He, B, O, and W, and where density profiles of all impurities have been assumed to be the same as those of the measured B density profiles. Impurities have been assumed to fulfil coronal equilibrium, computed within the ASTRA code [48]. Charge exchange with background neutral gas has not been included in the rate equations that determine the charge spectrum of the impurities. At mid–radius the heat flux produced by the calculated radiated power is about 21% of the total heating power in the NBI only heating phases, around 17% of the total heating power in the phases with additional

low ECH power, and it is only 11% of the total heating power in the phases with high ECH power. An uncertainty of 50% on the local value of the radiated power at mid–radius has been taken into account in the evaluation of the upper and lower values of the ratio of the anomalous particle flux to the total anomalous heat flux.

Finally, in Eq. (1), $Q_{i\mathrm{NC}}$ is the neoclassical ion heat flux and Γ_{Ware} the particle flux produced by the Ware pinch, both evaluated consistently at mid–radius. Neoclassical calculations have been performed with both NCLASS [49] and with formulae from [50], and good agreement has been found. It is found that under the conditions of the present shots, the flux produced by the Ware pinch is between 40% and 50% of the contribution provided by the beam particle source in the phases with NBI heating only, and it is only 20% in the phases with strong ECH, and, therefore, with increased electron temperature and reduced loop voltage. The ion heat flux produced by neoclassical transport is already well below 10% of the total heat flux at the radial location considered, in all phases.

Figure 6 shows an example of the solution to Eq. (1), obtained by scanning the value of R/L_{ne} in the numerical simulations. The ratio between particle flux and total heat flux obtained in the gyrokinetic calculations is plotted as a function of the value of R/L_{ne} used as an input. Three representative cases are shown, one for the heating phase with NBI only (squares), one for the phase with NBI and low central ECH power (triangles pointing down), and one for the heating phase with NBI and high central ECH power (triangles pointing up). Local magnetic equilibrium parameters do not change significantly with the application of ECH power, the local safety factor is between 2 and 2.2 and the magnetic shear increases with increasing ECH power from 0.8 with NBI only, to 0.9 with low ECH power and 1.0 with large ECH power, while the plasma shape is unchanged, with local elongation $k = 1.4$ and triangularity $\delta = 0.05$. The full symbols with error bars connected by solid lines show the results of nonlinear GYRO simulations, while open symbols connected by dashed lines show the corresponding results of linear GS2 calculations. The error bars plotted on the nonlinear results show one standard deviation of the fluctuations of the fluxes.

The comparison between quasi–linear and nonlinear results shows that, particularly in the cases with NBI heating only (squares) and with low ECH power (triangles pointing down), quasi–linear calculations predict larger ratios of the particle flux to the total heat flux at small values of R/L_{ne}. This is often the consequence of the fact that, particularly at large wave numbers, the quasi–linear phase shifts between electron density and electrostatic potential fluctuations do not follow closely the corresponding nonlinear ones, as shown by recent detailed comparisons between quasi–linear and nonlinear spectra [51, 52, 53]. In contrast, in the case with high ECH power (triangles pointing up), the sharp transition obtained in the quasi–linear results from strongly inward particle fluxes at values of $R/L_{ne} \leq 3.5$ to an outward flux at $R/L_{ne} = 4.5$ is produced by a transition from dominant ITG modes to dominant TEM instabilities with increasing R/L_{ne}, where only the most unstable modes at each wave number are considered in the quasi–linear transport model. The nonlinear results can be expected to produce a more continuous transition from one turbulence regime to the other. It can be also speculated that the ITG regime might persist longer in the nonlinear simulations with increasing

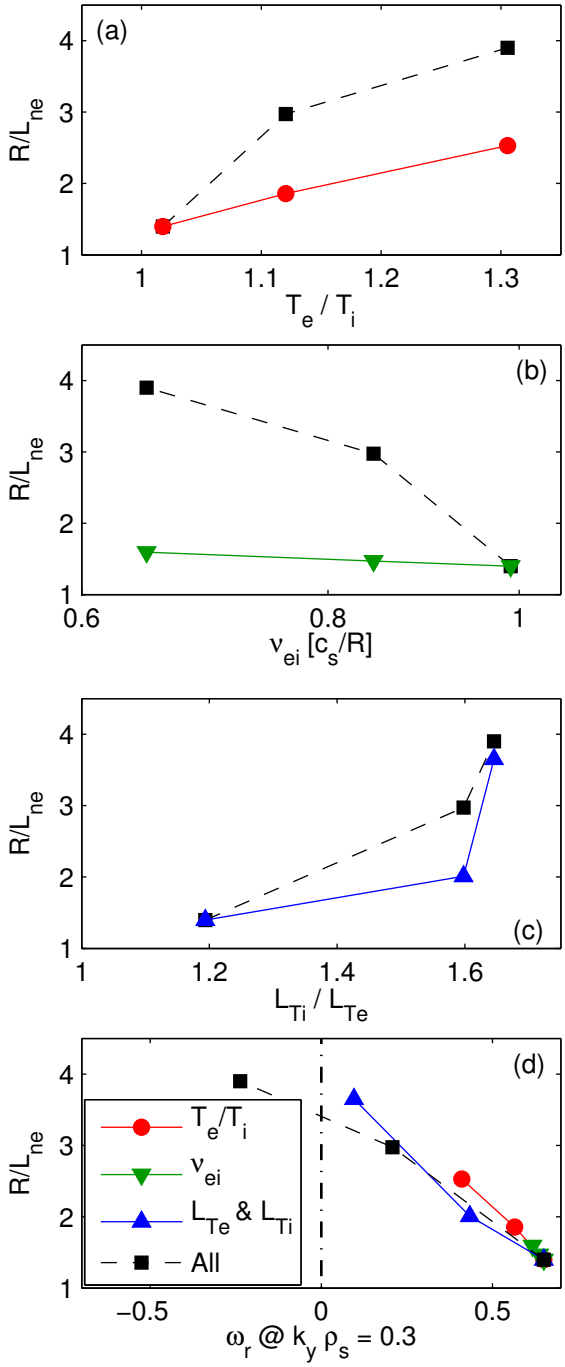

Figure 8. Predicted value of R/L_{ne} obtained by changing a single parameter at a time, (a) the electron to ion temperature ratio T_e/T_i (circles), (b) the collision frequency ν_{ei} (triangles pointing down), (c) the pair of logarithmic temperature gradients $(R/L_{Te}, R/L_{Ti})$ (triangles pointing up), and compared to the results obtained by changing all parameters simultaneously (squares), as a function of the corresponding varied parameter. The values of the varied parameters are taken from representative cases of the three heating phases, with NBI only for the lowest values of T_e/T_i and L_{Ti}/L_{Te} and the largest value of ν_{ei}, with NBI and low ECH power for all of the intermediate values, and with NBI and high ECH power for the largest values of T_e/T_i and L_{Ti}/L_{Te} and the lowest value of ν_{ei}. In (d), the predicted values of R/L_{ne} are plotted as a function of the corresponding values of the real frequency ω_r of the most unstable mode at $k_y\rho_i = 0.3$.

R/L_{ne}, due to the upshift of the nonlinear threshold of the density gradient driven TEM [54].

The gyrokinetic results provide the left hand side of Eq. (1). The horizontal lines show the corresponding right hand side of Eq. (1), where upper and lower dashed lines correspond to the error bar in this quantity, mainly reflecting the uncertainty in the profile of the radiated power density. This implies an uncertainty in $\Delta(R/L_{ne})$ of around 0.3 for the NBI heated only cases, around 0.16 for the cases with low ECH power, and only 0.05 for the case with strong ECH heating. Despite the differences between quasi–linear and nonlinear results, quasi–linear calculations match the experimental ratios of the particle flux to the total heat flux at values of R/L_{ne} which are rather close to those identified by the nonlinear simulations. We observe as well that the value of R/L_{ne} obtained in the absence of any fuelling and Ware pinch, that is the value at which $\Gamma_{n\,\mathrm{trb}} = 0$, is below 1 for the case with NBI heating only. This is significantly lower than the value which matches the actual turbulent particle to heat flux ratio, which in this specific case is $R/L_{ne} = 1.86$. This leads to the conclusion that in these relatively high collisionality conditions the combined contribution of NBI fuelling and the Ware pinch can provide a $\Delta(R/L_n)$ of around 1. In contrast, in the low collisionality case with high ECH power, the value of R/L_{ne} fulfilling the condition of $\Gamma_{n\,\mathrm{trb}} = 0$ is around 3, and therefore only $\Delta(R/L_{ne}) = 0.3$ smaller than the value of R/L_{ne} which matches the actual turbulent particle to heat flux ratio ($R/L_{ne} = 3.32$). These considerations allow us to conclude that the impact of the beam particle source and the Ware pinch becomes smaller in the high ECH power phases, at lower collisionality, while it can be significant in high collisionality regimes. This confirms a previous result obtained with theory–based transport modelling [20]. A non–negligible role of the Ware pinch has also been found in the gyrokinetic modelling of high collisionality plasmas in Alcator C–Mod [54].

Figures 7(a) and 7(b) show the results of the gyrokinetic modelling by means of linear calculations over the entire dataset, and by means of nonlinear simulations for the three representative cases already presented in figure 6. The predicted values of R/L_{ne} (full symbols) are compared to the actual measurements (open symbols) as a function of the measured value of T_e/T_i in figure 7(a). In figure 7(b), the same comparison between predicted and measured R/L_{ne} is plotted as a function of the real frequency of the most unstable mode at $k_y\rho_i = 0.3$ obtained from the linear calculations. Again, open symbols show the experimental values, plotted against the real frequency computed using the experimentally measured values of R/L_{ne} as inputs. The full symbols show the predicted values, plotted against the real frequency of the mode obtained using the predicted values of R/L_{ne} as inputs. The real frequency at the wave number $k_y\rho_i = 0.3$ is used in figure 7(b) since this is the value of $k_y\rho_i$ around which, in most cases, the linear growth rate is maximum and also because this wave number is representative of the spectral region where the peak of the particle transport is produced in nonlinear simulations, as it will be shown in Fig. 10. The quantitative agreement between the predicted values and the measured values of R/L_{ne} is good. In the quasi–linear results, the mean deviation between experimental and predicted values of R/L_{ne} is about 15% ($|\Delta(R/L_{ne})| = 0.33$)

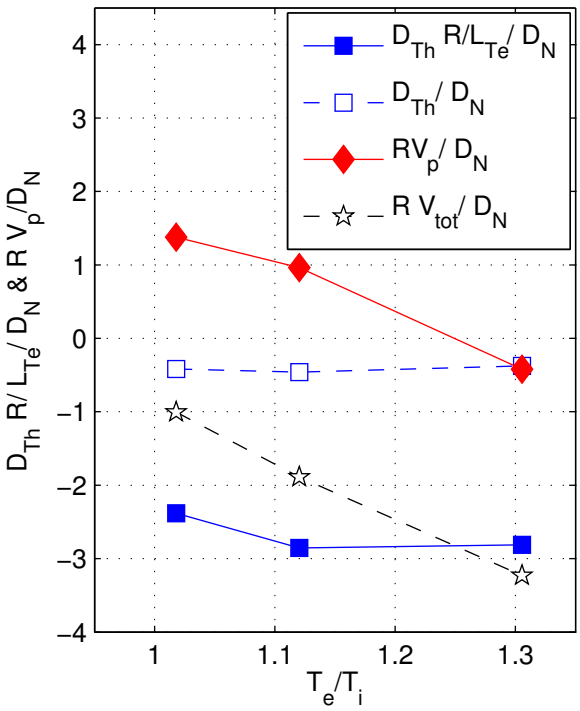

Figure 9. Electron thermodiffusive contribution (full squares) and thermodiffusive factor (open squares), as well as electron pure convection (full diamonds) as a function of the electron to ion temperature ratio for three representative cases of the different heating phases. The phase with NBI only has the lowest value of T_e/T_i, that with NBI and low ECH power has the intermediate value of T_e/T_i and the phase with NBI and high ECH power has the largest value of T_e/T_i. Open stars show the sum of the two contributions, thermodiffusion (full squares) and convection (full diamonds).

for the cases with NBI heating only, about 30% ($|\Delta(R/L_{ne})| = 0.80$) for the cases with low ECH power, and only 10% ($|\Delta(R/L_{ne})| = 0.39$) for the cases with high ECH power. Despite this overall good agreement, we note that rather large disagreements are found in a few specific cases, which can be as high as 50% ($|\Delta(R/L_{ne})| = 1.1$). In the three cases modelled by the nonlinear GYRO simulations, the agreement with the corresponding experimental data points remains within 20%, a result which in our view can be considered indeed satisfactory. In addition, it is important to underline that the theoretical predictions reproduce the dependence of the experimental measurements on various plasma parameters, and in particular those as a function of the electron to ion temperature ratio or as a function of collisionality (not shown). We note also that, as illustrated in figure 6, the right hand side of Eq. (1) decreases with increasing ECH power. This clearly indicates that the observed dependence of the density peaking has to be accounted for by a variation of the left hand side of the same equation. That is to say, it cannot be explained by means of neoclassical or particle source effects, but must be a consequence of a turbulent transport mechanism.

Figure 7(b) shows the real frequencies ω_r of the most unstable modes at $k_y\rho_i = 0.3$. The real frequency is found to reverse sign in the cases with strong central ECH (triangles

pointing up). The investigation of the linear spectra reveals that the values of ω_r are positive, for all cases with NBI only and with additional low ECH power. That is to say, ITG modes are the most unstable modes over the entire wave number spectrum considered. In constrast, in phases with large central ECH power, the most unstable modes are found to be TEM (negative ω_r) over the entire wave number spectrum considered for most cases and in a few cases over the range of wave numbers from $k_y\rho_i = 0.1$ to $k_y\rho_i = 0.6$, with a transition to positive frequencies for larger values of $k_y\rho_i$, but with lower values of the growth rate. Figure 7(b) shows that both the predicted and the experimental values of R/L_{ne} are well ordered by the real frequency of the mode. This property of the real frequency of the unstable modes with respect to the peaking of the electron density profile was already suggested in [10] and has been fully explored more recently in [55]. In the present work we provide a clear demonstration of this property, under the plasma conditions considered here. In this context, it is of interest to compare figure 7(b) with figure 3(a,d) in [10] and with figure 7(a) in [55]. Consistent with previous studies [7, 8, 10, 12], an increase of density peaking in response to the application of central ECH is observed when the most unstable modes identified by linear gyrokinetic calculations are ITG modes. In the regime at the transition between ITG and TEM, the largest predicted values of R/L_{ne} are obtained. Moving further in the TEM instability domain, and increasing further the absolute value of the real frequency, a decrease of R/L_{ne} is predicted to occur. This theoretical prediction cannot be validated by the present experimental results, but motivates further experimental studies on the same type of H–mode plasmas in future AUG campaigns, in which a larger amount of ECH power will be available as compared to that used in the present experiments. As already mentioned in the introduction, this theoretically predicted mechanism for density flattening in the TEM turbulence regime has already been proposed to explain the observation of density "pump–out" with central electron heating, which is regularly observed in low density L–mode plasmas [7, 8, 10, 12].

A deeper understanding of the transport mechanism responsible for the increase of the peaking of R/L_{ne} in the gyrokinetic simulations, and likely also in the experiment, can be obtained using an expression of the particle flux which can be derived from a formal solution of the linearized gyrokinetic equation. The derivation of this expression can be found in the previous literature (e.g. in [51, 55] and in [1] and references therein), and will not be reported here. The quasi–linear electron particle flux can be expressed in the following form [1],

$$\Gamma_{QL} = \sum_k \frac{k_y c_s^2}{\Omega_{ci}} \left\langle \int d^3v F_M \frac{(\hat{\gamma}_k + \hat{\nu}_k)[R/L_n + (E/T_e - 3/2)R/L_{Te}] - (\hat{\gamma}_k \hat{\omega}_{Gk} - \hat{\omega}_{rk}\hat{\nu}_k)}{(\hat{\omega}_{rk} + \hat{\omega}_{Gk})^2 + (\hat{\gamma}_k + \hat{\nu}_k)^2} J_0(k_\perp \rho_s)^2 |\hat{\phi}_k|^2 \right\rangle, \quad (2)$$

where γ_k and ω_{rk} are the growth rate and real frequency of the unstable linear mode, $\hat{\omega}_{Gk} = k_\parallel v_\parallel + \omega_{dk}$ is the kinetic frequency comprising both parallel and perpendicular motion, and all frequencies are normalized to the fluid perpendicular drift frequency $\omega_{Dk} = k_y \rho_s c_s / R$. The normalized collision frequency is $\hat{\nu}_k = \nu_{ei}(v_{the}^3/v^3)/\omega_{Dk}$, where ν_{ei} is the fluid collision frequency. The sign convention is that a positive value for the real frequency $\hat{\omega}_{rk}$ identifies a mode propagating in the ion diamagnetic direction, that is, an

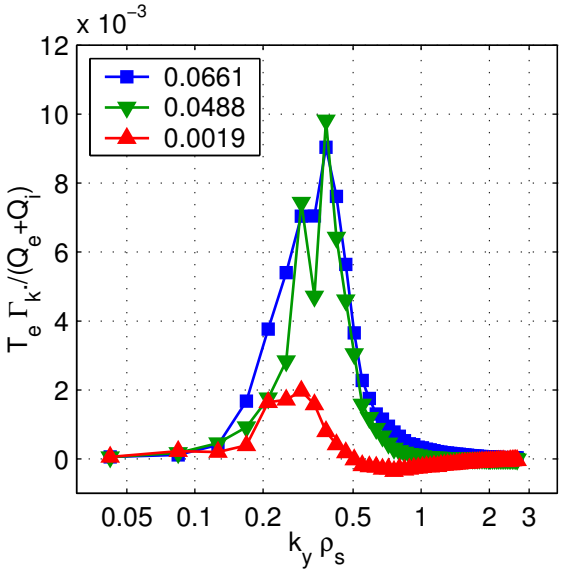

Figure 10. Binormal wave number spectra of the particle flux normalized to the total heat flux obtained in three GYRO nonlinear simulations, with fixed value of $R/L_{ne} = 3$, and other input parameters taken from measurements from representative cases of the three different heating phases, with NBI heating only (squares), with NBI and low central ECH (triangles pointing down) and with NBI and high central ECH (triangles pointing up). Values in the legend provide the corresponding ratio of the total particle flux to the total heat flux.

ITG. Such an expression for the particle flux can be also written in the more compact form,

$$\frac{R\Gamma_{ntrb}}{n_e} = D_N \frac{R}{L_{ne}} + D_{Th} \frac{R}{L_{Te}} + RV_p, \tag{3}$$

where the turbulent particle flux is decomposed in diffusive, thermodiffusive and pure convective contributions, and where the definition of the transport coefficients in terms of the kinetic expression given by Eq. (2) is straightforward.

From Eq. (2) we observe that, as already noted in previous works [51, 55], the effect of collisions on the electron particle flux can be considered as an additional convective term that is directed outward for modes propagating in the ion drift direction (positive value of ω_r) and which decreases with decreasing values of ω_r. A reduction of collisionality by itself produces a reduction of ω_r. Therefore, with a decrease of collisionality, the term $\hat{\omega}_{rk}\hat{\nu}_k$ in Eq. (2) decreases for the concomitant effect of a reduction of ν_{ei} and the consequent reduction of ω_r. However, in the case of the present experiments the reduction of ω_r is not produced only by a reduction of ν_{ei}, but also by a concurrent increase of T_e/T_i and L_{Ti}/L_{Te}. An additional effect which can be produced by a decrease of the real frequency ω_r, particularly if in combination with an increase of R/L_{Te} like in the present cases, is the increase of the thermodiffusive term. This term is proportional to R/L_{Te}, is directed inward for ITG modes [7, 1, 56], and increases in size when the frequency approaches zero, since by this it increases the contribution of slow particles, which flow inward at energies $E/T_e < 3/2$.

These considerations allow us to conclude that in the case of the experimental results analyzed in the present work, the observed density behaviour cannot be explained by a reduction of collisionality alone. Actually, given the rather limited variation in collisionality, collisionality turns out not to be the most important player here. More important is the concurrent modification of other plasma parameters, where none can be neglected in order to match the experimentally measured dependence. A demonstration of this can be obtained by considering a reference case with NBI only, and by producing a set of calculations in which only one parameter among T_e/T_i, ν_{ei}, and the pair of logarithmic gradients (R/L_{Ti} , R/L_{Te}) is varied at a time from its nominal value in the NBI phase to the measured values in the other heating phases, i.e. with low and with high ECH power. In figure 8(a-c) the results of these simulations are compared to the case in which all three parameters are changed simultaneously. No parameter alone can reproduce the experimental dependence, which is well reproduced when all the parameters are modified concurrently. The dominant role is clearly played by the pair of logarithmic gradients (R/L_{Ti} , R/L_{Te}), followed by the electron to ion temperature ratio T_e/T_i, whereas the limited variation in collisionality has a much weaker effect. The increase of the predicted R/L_{ne} with increasing R/L_{Te} has been shown also in global nonlinear gyrokinetic simulations [57], whereas a quantitative comparison between predicted and measured values of R/L_{ne} in JET plasmas particularly dedicated to the dependence on collisionality has been presented in [35]. As demonstrated in figure 8(d), the impact of the variation of each parameter on the predicted value of R/L_{ne} is directly measured by the shift in real frequency that it produces. Here again the shift in frequency exhibits a clear correlation with the corresponding increase of the predicted value of R/L_{ne}.

The concurrent modification of several plasma parameters produced by central ECH implies that non–negligible modifications of both the pure convective term RV_p and the thermodiffusion D_{Th} are taking place at the same time. It is worth noting that the pure convective term comprises both the collisionless component, which includes the so–called curvature pinch [21] and is proportional to $\hat{\gamma}_k\hat{\omega}_{Gk}$ in Eq. (2), and the collisional component, which is proportional to $-\hat{\omega}_{rk}\hat{\nu}_k$ in Eq. (2) [51, 55]. These convective and thermodiffusive contributions to the electron particle flux have been calculated specifically for three representative cases and are shown in figure 9. The pure convection is directed outward (diamonds) in the NBI only and low ECH cases, due to the outward directed contribution provided by collisions in Eq. (2), and decreases with increasing T_e/T_i (increasing central ECH power), due to its dependence on ω_r. In contrast, it is directed inward (negative) in the high T_e/T_i case, due to the reversal of the sign of the real frequency. The thermodiffusion factor D_{Th}/D_N (open squares) is almost constant in the three heating phases, and negative, as expected for ITG modes and for TEMs at small real frequencies. Since the thermodiffusion contribution to R/L_{ne} is multiplied by R/L_{Te} (full squares), which significantly increases with the application of central ECH, the inward contribution produced by thermodiffusion also increases with increasing central ECH power from the NBI case to the low ECH case. In contrast, we note that due to the transition to dominant TEM in the high ECH phase, the

thermodiffusion contribution $(D_{Th}/D_N)(R/L_{Te})$ remains practically constant from the low ECH case to the high ECH case (despite the increase of R/L_{Te} in the high ECH phase), since in TEM the thermodiffusion coefficient D_{Th}/D_N decreases in size with increasing absolute value of the real frequency. In conclusion, the observed increase of R/L_{ne} with increasing central ECH power is explained by a concurrent reduction of the outward pure convection, which eventually becomes directed inward in the high ECH phases with dominant TEM, and an increase of the inward thermodiffusion. Open stars in figure 9 show the predictions of $-R/L_{ne}$ obtained by directly summing these two contributions, that is the values of R/L_{ne} identified by linear extrapolation of the particle flux dependence on the gradients at the condition $\Gamma_{n\,\mathrm{trb}} = 0$, where $R/L_{ne} = -(D_{Th}/D_N)(R/L_{Te}) - (RV_p/D_N)$.

We turn now to the nonlinear results, and we show in figure 10 the binormal wave number k_y spectra of the particle flux for three nonlinear gyrokinetic simulations. These simulations have been performed at the same value of $R/L_{ne} = 3$, but with all other input parameters taken from three representative cases of our dataset, one with 5 MW of NBI heating only, one with additional low ECH power, and one with additional high ECH power. From the results obtained so far, it can be expected that at such a relatively large value of R/L_{ne}, the first two cases will have a particle flux directed outward, whereas the last case will be at a condition in which the particle flux is practically zero. The results are presented in figure 10, where the contribution per toroidal mode Γ_k to the total particle flux, normalized to the total heat flux, is plotted. In the legend, the corresponding values of the ratio of the total particle flux to the total heat flux are presented. We observe that the condition of a particle flux at the experimental value, that is almost at the null, is obtained by a combination of two effects. The level of the particle flux becomes smaller, and in addition a compensation between large scales flowing outward and small scales flowing inward takes place. These results show an application to these specific cases of the characteristics of a turbulent plasma state which produces a particle flux at the null, already documented in [51]. The reduction of the level of the particle flux obtained in the case with large ECH power, despite the same value of the logarithmic density gradient $R/L_{ne} = 3$ is used as an input, is due to a combination of two effects. At each wave number, there is a compensation of contributions in the velocity space, where particles at low energy flow inward and particles at large energies flow outward. In addition, another compensation mechanism takes place at different scales, due to the different impact of collisionality, which is much stronger at large scales, which flow outward, with respect to small scales, which can be directed inward [51].

Finally, although the present work is not dedicated specifically to the study of heat transport, an important verification of the applicability of the present gyrokinetic modelling to the particle transport channels is provided by the comparison of the predicted ratio of the electron or ion heat flux to the total heat flux with the experimental levels. This comparison is important because this ratio is one of the most direct quantities at a macroscopic level which reflects the characteristics of the type of turbulence present in the plasma, in particular ITG or TEM, and the impact

of the trapped electron response in ITG turbulence. In the present simulations, no adjustment of the electron and ion logarithmic temperature gradients has been applied within the respective experimental uncertainties in order to match the experimental heat flux values evaluated by power balance analysis. Despite this, the gyrokinetic simulations deliver values of the local ratio of the ion heat flux to the total heat flux which are in satisfactory agreement with the power balance values. In the specific case of the nonlinear GYRO simulations, an agreement within 10% is found, which is indeed satisfactory ($Q_{i\,\mathrm{trb}}/Q_{tot\,\mathrm{trb}}$ from GYRO is 0.68 for the NBI only phase, 0.63 for the low ECH power phase and 0.54 for the high ECH power phase, while the power balance values are 0.77, 0.64 and 0.54 respectively, with error bars around 15%). In addition, it is of interest to compare the actual levels of heat fluxes predicted by the nonlinear simulations with those present in the experiments and evaluated by power balance analysis. It is found that the ratio of the total turbulent heat flux predicted by GYRO to the total anomalous heat flux present in the experiments is 1.35 for the NBI only phase, 1.18 for the phase with additional low ECH power, and 1.05 for the phase with additional high ECH power. This shows that the present nonlinear GYRO simulations produce heat fluxes which are very compatible with the actual anomalous heat fluxes present in the experiments.

In the case of quasi–linear GS2 calculations, the agreement is not as good in the cases with strong ECH. In these cases the electron heat flux is largely overestimated (in the GS2 quasi–linear calculations $Q_{i\,\mathrm{trb}}/Q_{tot\,\mathrm{trb}}$ is around 0.7 in the NBI only phases, around 0.6 in the low ECH phases, values which are in good agreement with the power balance, but it is only 0.3 in the strong ECH phases, in clear disagreement with the experimental values). This was partly to be expected, since only the dominant contribution of the most unstable linear mode, the TEM, is considered in these quasi–linear calculations, while the subdominant contribution of the ITG modes, which is important to produce the ion heat flux, is neglected.

4. Modelling of R/L_{nB}

We turn to the modelling of the normalized logarithmic density gradients R/L_{nB} of the boron profiles. The conclusions drawn in the previous section on the type of dominant instabilities and turbulence, which are responsible for the behaviour of the electron density, become at this stage a constraint for the modelling of the boron profiles, since the modelling of the impurity must be consistent with that of the main plasma. In particular, we note that in the modelling of R/L_{nB}, the parameter R/L_{ne} becomes an input to the gyrokinetic calculations. Hence, a choice has to be made about whether it is more appropriate to use the experimentally measured values of R/L_{ne} or the theoretically predicted ones. Given the good agreement between predicted and experimental values of R/L_{ne} shown in figure 7, the calculations for boron can be performed with either the experimental or the predicted values of R/L_{ne}. We performed both set of simulations. In this section, we present the results obtained using the experimental values of R/L_{ne} as inputs. The results obtained with the predicted values

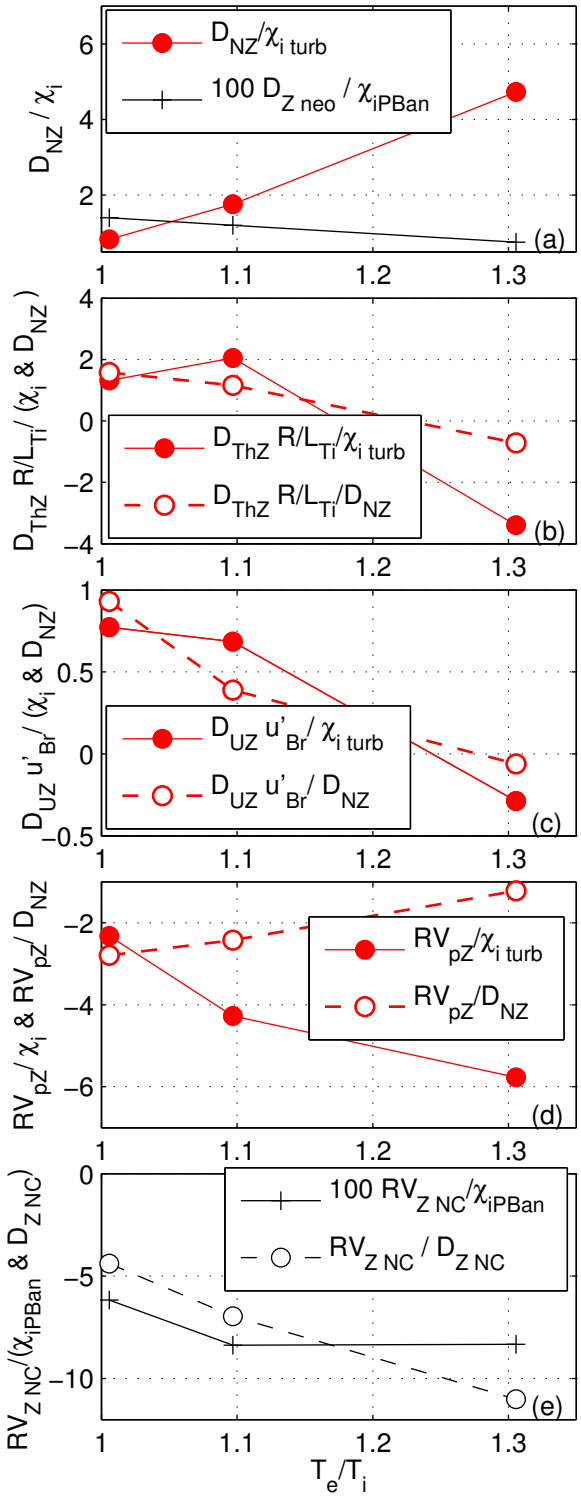

Figure 11. Neoclassical and turbulent contributions to the boron transport as a function of the electron to ion temperature ratio T_e/T_i. Turbulent contributions are plotted normalized to both the turbulent effective ion heat conductivity (full circles and solid lines) and the turbulent boron diagonal diffusivity (open circles and dashed lines). Neoclassical contributions are normalized to the power balance anomalous ion heat conductivity (crosses and solid lines) and to the neoclassical diagonal diffusivity (open circles and dashed lines). (a) Turbulent and neoclassical diffusion coefficients, (b) turbulent thermodiffusive contribution, (c) turbulent roto–diffusive contribution, (d) turbulent pure convection and (e) total neoclassical convection are plotted.

of R/L_{ne} as inputs are presented in the Appendix for direct comparison. Very similar results have been obtained.

In the modelling of impurity transport we initially consider both turbulent and neoclassical components. The neoclassical transport of boron has been computed with NCLASS [49], implemented inside the ASTRA code [48], which was run in interpretative mode. The same impurities that were used in the calculation of the radiated power density profile were included in the NCLASS calculations. The turbulent and neoclassical components have been added together, and the normalized logarithmic density gradient of boron R/L_{nB} has been identified by the condition at which the total boron particle flux is zero. In stationary conditions, this implies that R/L_{nB} is given by the following expression

$$\frac{R}{L_{nZ}} = -\frac{RV_{Z\,\mathrm{trb}} + RV_{Z_{\mathrm{NC}}}}{D_{NZ\,\mathrm{trb}} + D_{NZ_{\mathrm{NC}}}}, \tag{4}$$

where the sum of the total turbulent and neoclassical convections, $RV_{Z\,\mathrm{trb}}$ and $RV_{Z\,\mathrm{NC}}$, are divided by the sum of the turbulent and neoclassical diffusivities, $D_{NZ\,\mathrm{trb}}$ and $D_{NZ_{\mathrm{NC}}}$. At this point, the values of both the turbulent and the neoclassical transport coefficients can be computed and added as indicated in Eq. (4). However, this procedure cannot be considered particularly reliable, since it is well known that the turbulent transport levels obtained in simulations are highly sensitive to the values of the temperature gradients used as inputs and, within the experimental uncertainties, the resultant simulated turbulent fluxes can be an order of magnitude larger (or smaller) that those actually present in the experiment. This would lead to a consequent underestimate (or overestimate) of the contribution provided by neoclassical transport. To overcome this limitation, a more appropriate procedure is employed, in which a normalization is introduced that ensures that the turbulent flux levels are renormalized to the experimental ones when the transport coefficients of the turbulent and the neoclassical contributions are added together. Suitable coefficients which can be used in this normalization procedure are effective, electron, ion heat conductivities. This procedure assumes that the ratio of an impurity transport coefficient to an effective heat conductivity is weakly dependent on the actual level of turbulent transport, provided that the main characteristics of the driving instabilities and turbulence are preserved, an assumption whose applicability has been verified [58]. In this work, the following formula has been applied to combine turbulent and neoclassical transport,

$$\frac{R}{L_{nZ}} = -\frac{RV_{Z\,\mathrm{trb}}/\chi_{i\,\mathrm{trb}} + RV_{Z\mathrm{NC}}/\chi_{i\,\mathrm{PBan}}}{D_{Z\,\mathrm{trb}}/\chi_{i\,\mathrm{trb}} + D_{Z\mathrm{NC}}/\chi_{i\,\mathrm{PBan}}}, \tag{5}$$

where $\chi_{i\,\mathrm{trb}}$ is the effective ion heat conductivity obtained in the gyrokinetic calculation, and $\chi_{i\,\mathrm{PBan}} = \chi_{i\,\mathrm{PB}} - \chi_{i\,\mathrm{NC}}$ is the anomalous part of the power balance ion heat conductivity, given by the difference between the actual power balance ion heat conductivity and the neoclassical ion heat conductivity. The normalizations of the turbulent and the neoclassical contributions to the impurity transport by the predicted and the experimental anomalous heat conductivities presented in Eq. (5) are particularly suited for the application of quasi–linear calculations of turbulent transport, but they

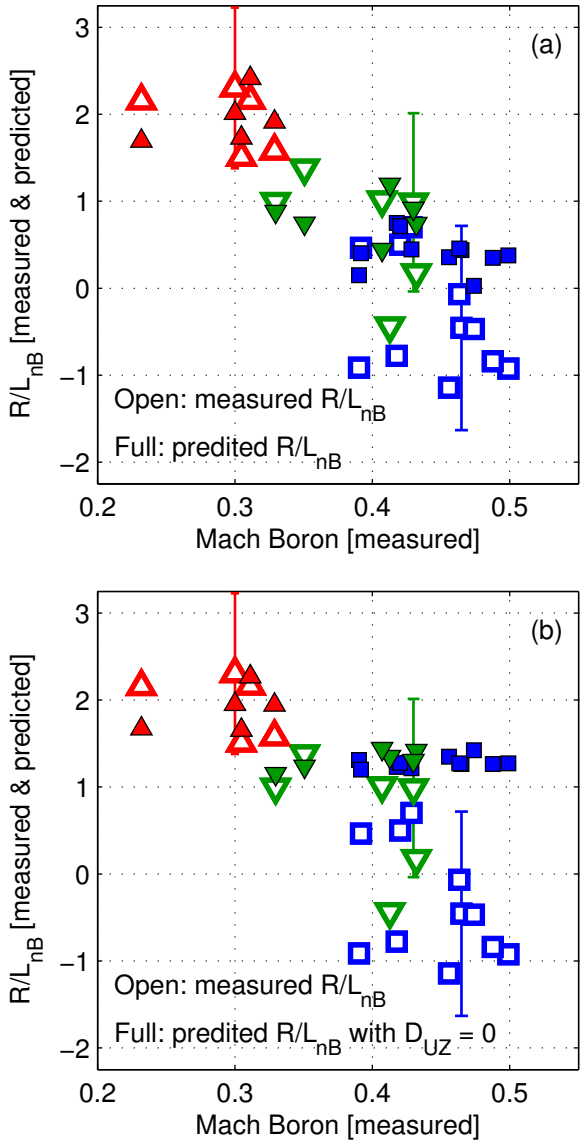

Figure 12. (a) Predicted (full symbols) and measured (open symbols) values of the normalized logarithmic boron density gradient R/L_{nB} as a function of the boron Mach number, for the entire dataset, with NBI heating only (squares), with NBI and low central ECH (triangles pointing down) and with NBI and high central ECH (triangles pointing up). In (b), the same quantity is plotted as in (a), but excluding the contribution from roto–diffusion, that is with $D_{UZ} = 0$ in Eq. (6). Numerical results are obtained from quasi–linear GS2 calculations.

are also of practical interest for applications with nonlinear simulations. As already pointed out above, any mismatch on the predicted turbulent heat fluxes against the actual experimental power balance fluxes can be corrected by the normalizations, which practically force the turbulent heat flux to be the same as the anomalous power balance heat flux.

While the impact of the toroidal rotation and its radial gradient is negligible on electron particle transport, this can become important for impurities, due to their

heavier mass and lower thermal velocity [59]. For this reason, it has been included in this work in the gyrokinetic calculations of boron transport. Then, the expression for the turbulent boron particle flux can be decomposed in the following way [59],

$$\frac{R\Gamma_{nZ}}{n_Z} = D_{NZ}\frac{R}{L_{nZ}} + D_{ThZ}\frac{R}{L_{TZ}} + D_{UZ}u'_Z + RV_{pZ}, \tag{6}$$

where in addition to diagonal diffusion D_{NZ}, thermodiffusion D_{ThZ} and pure convection RV_{pZ} [60, 61, 62, 63, 64], an additional off–diagonal contribution is present, proportional to the gradient of the toroidal velocity, and which we shall call roto–diffusion. Comparing Eq. (6) with Eq. (5), we easily identify that $D_{Z\,\mathrm{trb}} = D_{NZ}$ and that the total turbulent convection $RV_{Z\,\mathrm{trb}}$ is given by $RV_{Z\,\mathrm{trb}} = D_{ThZ}R/L_{TZ} + D_{UZ}u'_Z + RV_{pZ}$. The different contributions to the turbulent transport have been computed with quasi–linear gyrokinetic calculations using the code GS2, in the limit of small boron concentration, which implies that Eq. (6) becomes perfectly linear. We verified that this limit is adequate to describe the experimental conditions, by noting that the boron concentrations are around 1% in these discharges, as shown in figure 2. We mention also that boron is the only impurity included in these gyrokinetic calculations. The good agreement found between linear and nonlinear simulations of He transport in a previous work [58] suggested to limit the modelling of impurity transport to linear calculations only. The version of GS2 which has been used for these calculations includes both the radial gradient of the rotation, as in the original version of the code, as well as the rotation itself [65], and keeps terms only to the first power of the Mach number. This implementation has been made following the formulation of the gyrokinetic equation in the plasma rotating frame described in [66]. In this frame, the radial gradient of the toroidal velocity becomes $u'_{Zr} = (R^2/v_{thZ})d\Omega_Z/dr$, where Ω_Z is the toroidal angular rotation velocity, and the rotation enters the gyrokinetic equation producing the additional Coriolis drift [67]. In [65] the rotation terms added to GS2 were benchmarked with GYRO and GKW [68]. Centrifugal effects [69] have not been included in GS2 and have been neglected in the present calculations. The maximum values of M_B^2 achieved in the experiments considered here are below 0.25, and it can be expected that centrifugal effects will produce only a minor correction to boron turbulent fluxes which already include first order terms in M_B, like those computed here (figure 10 in ref. [59] shows a specific comparison obtained with a reduced fluid model, in which centrifugal effects on carbon are found to be practically negligible for deuterium Mach numbers below 0.25, like those obtained in the plasmas considered in this work). However, for heavier impurities centrifugal effects can be expected to become significant. In addition, as we shall see, compensations can take place between the different contributions of the off–diagonal turbulent transport, which can be in opposite directions, which means that small terms, like those due to second order rotational effects, can still play a significant role. Finally, it is important to underline that a symmetry breaking mechanism for the eigenfunction of the unstable mode is required for the roto–diffusion coefficient D_{UZ} to be non–zero, since otherwise this coefficient would result from the flux surface average of an anti–symmetric function in the poloidal angle θ, and therefore, would vanish. The mechanism which produces

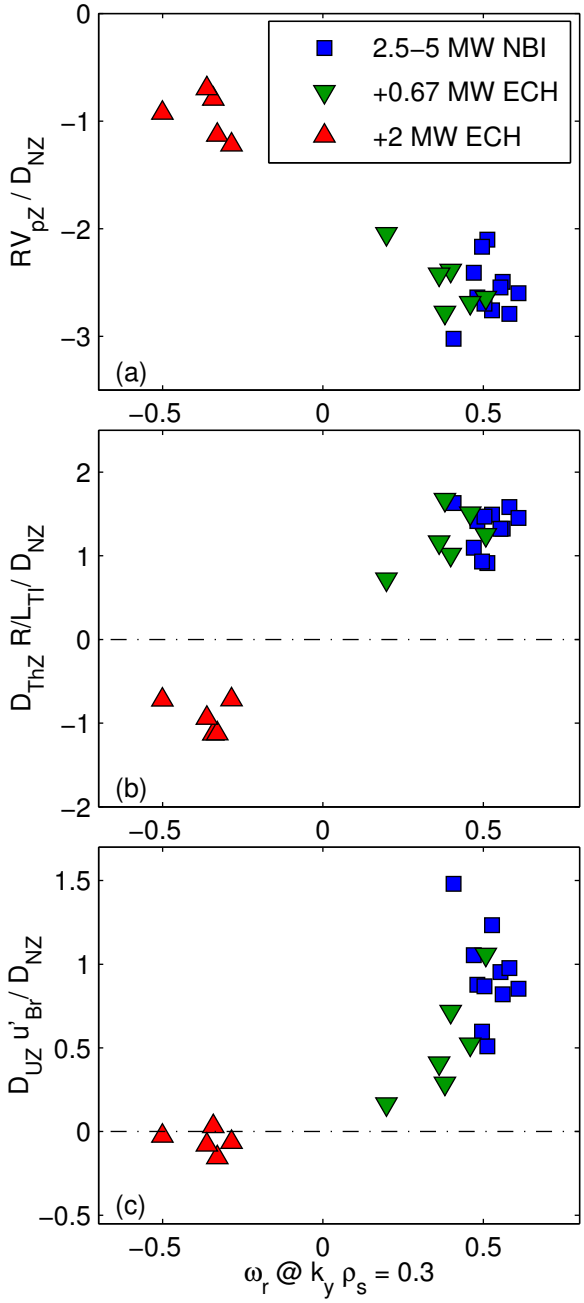

Figure 13. Turbulent off–diagonal contributions to boron transport, (a) pure convection, (b) thermodiffusion, and (c) roto–diffusion, normalized to the diagonal diffusivity, obtained by quasi–linear calculations with GS2, as a function of the frequency ω_r of the most unstable mode at $k_y \rho_i = 0.3$ for the entire dataset, with NBI heating only (squares), with NBI and low central ECH (triangles pointing down) and with NBI and high central ECH (triangles pointing up).

an asymmetry in the eigenfunction of the mode is provided by the concurrent toroidal rotation of the deuterium and by its radial gradient. The latter has been evaluated from the experimental measurements of the toroidal rotation of boron with NCLASS. The different terms occurring in Eqs. (5) and (6) are shown in figure 11 for the usual

three representative cases. First of all, in figure 11(a) and 11(e), we observe that the neoclassical contributions are small compared to the turbulent ones, which is a rather generic result in tokamak plasmas around mid–radius. In addition, predictions based on neoclassical transport alone yield values of $R/L_{nB\,\mathrm{NC}} = -RV_{Z\,\mathrm{NC}}/D_{Z\,\mathrm{NC}}$ much more peaked than those observed in the experiment. It is evident, therefore, that the observations cannot be explained by neoclassical transport alone, and that they are mainly produced by anomalous (turbulent) transport processes.

The turbulent transport coefficients of boron present a set of interesting features. The ratio of the boron turbulent diffusion to the ion heat conductivity, figure 11(a), increases strongly from the case with NBI heating only, $T_e/T_i \simeq 1$, to the case with additional high ECH power, $T_e/T_i \simeq 1.3$. The thermodiffusion, figure 11(b), is directed outward in the NBI only and low ECH cases, which is to be expected for ITG modes, and is therefore in the opposite direction with respect to the thermodiffusion of electrons, figure 9. In contrast, it is directed inward in the high ECH case, since in this case a TEM is dominant [62]. The same behaviour is exhibited by the roto–diffusion term, figure 11(c), which is directed outward in the cases with dominant ITG modes, whereas it is directed inward for the case with dominant TEM [59]. Finally, the pure convective term, figure 11(d), is directed inward for all cases. We observe also that the boron roto–diffusion and thermodiffusion terms are smaller than the pure convection. However, since they can both be of the same sign and opposite to the sign of the pure convection, the different contributions can partly balance each other, making the relative role of roto–diffusion more important.

The boron transport coefficients have been computed over the entire dataset, applying Eq. (5), and the predicted values of R/L_{nB} can be directly compared with those experimentally measured, as was done for R/L_{ne}. This comparison is shown in figure 12(a), as a function of the boron Mach number, with measured and predicted values plotted with open and full symbols, respectively. Although the agreement is not perfect, particularly for the cases with NBI heating only (squares), the general trend of the experimental results is well reproduced, with the boron profiles moving from rather flat in the case of NBI heated only plasmas (squares) to moderately peaked with high additional ECH power (triangles pointing up). We note, that the observed local hollowness of the boron density profiles observed in many cases with NBI only heating is not reproduced by the theoretical modelling, while the agreement is very good in the cases with ECH. This might suggest that our modelling is omitting a non–negligible contribution which is particularly important in the case of more strongly rotating plasmas. As we already mentioned, very flat or hollow profiles of relatively light impurities like boron or carbon appear to be a rather generic feature of typical H–mode plasma conditions [28, 29], which has not been satisfactorily explained by theory to date. In figure 12(b) an analogous comparison is presented, where this time the roto–diffusion coefficient has been set to zero, which allows us to show the impact of this specific term on the predictions. First of all, we observe that it is non–negligible, particularly for the NBI heated only plasmas, which have the largest values of rotation and rotation gradient. In addition, since it is directed outward in ITG turbulence, it

turns out to be an important ingredient to predict the experimentally observed trend of increasing boron density peaking with increasing ECH power. However, the combination of roto–diffusion and thermodiffusion, both directed outward in the ITG dominated NBI only heated cases, is not large enough to overcome the inward directed contribution provided by the pure convective term, and does not lead to the prediction of locally hollow profiles, which are observed in many cases in the phases with NBI heating only.

Since neoclassical effects turn out to be almost negligible, the predicted value of R/L_{nB} is practically given by the turbulent transport contributions only,

$$\frac{R}{L_{nB}} \simeq -\frac{D_{ThZ}}{D_{NZ}}\frac{R}{L_{TB}} - \frac{D_{UZ}}{D_{NZ}}u'_{Br} - \frac{RV_{PZ}}{D_{NZ}}.$$

We find it of interest to plot the three contributions as a function of the real frequency ω_r of the most unstable mode for the entire dataset, in figure 13. We observe that the roto–diffusion contribution, figure 13(c), is comparable in size to the thermo–diffusion contribution, figure 13(b), and clearly non–negligible, in the phases with NBI only heating (squares) and low ECH power (triangles pointing up). We observe also that the roto–diffusion contribution becomes close to zero during phases with large central ECH, due to the reduction and flattening of the rotation velocity profile. Another interesting aspect is to compare the thermodiffusion contribution of boron, figure 13(b), with that of electrons, figure 9. We note that in the phases with NBI heating only and with low ECH power (dominated by ITG modes) they have oppostite signs, which is a direct consequence of the charge dependence of the curvature and ∇B drift. However, the thermodiffusion contribution increases in size from the NBI only phase to the low ECH phase for electrons, while it decreases for boron. In contrast, in the high ECH power phase (dominated by TEMs) the thermodiffusion contribution decreases slightly for electrons, but remains inward, while it reverses sign for boron, becoming inward as well.

The different behaviours of the thermodiffusion contributions to electron and boron transport, and in particular how in some regimes thermodiffusion can be directed inward for both electrons and impurities, despite their opposite electric charge, deserve an explanation. This can be obtained from Eq. (2). In the presence of an ITG mode with a frequency close to zero, the electron thermodiffusion mechanism, arising from the inbalance between slow electrons moving inward and fast electrons moving outward, enhances the inward contribution of slow particles as long as the frequency is positive, or even when it becomes negative (TEM), but remains small in size. Actually the condition of the real frequency close zero at the transition between ITG and TEM leads to the largest inward contribution and the largest predicted values of peaking, as suggested here in figure 7(b) for instance, and as comprehensively demonstrated in [56, 55]. The electron thermodiffusion reverses sign from inward to outward into the TEM regime, provided that the mode frequency is sufficiently large in magnitude. This implies that electron thermodiffusion does not cross zero exactly at the transition from ITG to TEM ($\omega_r \simeq 0$), but rather at values of ω_r which are already negative, that is to say with a shift into the TEM domain [56]. For impurity ions, the situation is completely reversed. The shift in frequency at which the boron thermodiffusion crosses the null, changing direction

from inward, with TEMs, to outward, with ITGs, is slightly in the ITG instabilitiy domain and not exactly where ω_r crosses zero. We add that in this small frequency range in which thermodiffusion reverses direction, the thermodiffusion dependence on the real frequency becomes very steep [56]. Thermodiffusion moves from inward to outward at small but finite negative (TEM) frequencies for electrons, and from outward to inward at small but finite positive (ITG) frequencies for (sufficiently light) impurities (we remind the reader that thermodiffusion vanishes with increasing impurity charge, due to the inverse charge dependence of the vertical drift). This explains why TEMs with small frequencies can still produce a large inward thermodiffusion for electrons, enhanced by the strong values of R/L_{Te}, like those shown in figure 3(c), as well as an inward thermodiffusion for boron. It turns out that the fulfillment of this specific condition is the requirement for predicting correctly the observed values of R/L_{ne} and R/L_{nB} in phases with high additional ECH power. Hence, the achievement of real frequencies being negative, but sufficiently close to zero, in the phases with high ECH power allows concurrently not only an inward thermodiffusion for boron, but also, and more critically, a significant inward thermodiffusion for electrons.

The considerations in the previous paragraph provide an example of investigations, in which both electron and impurity density profiles are modelled concurrently, and by which observations in both transport channels provide complementary and more stringent conditions on the identification of the turbulent state which can explain the experimental observations in both the transport channels.

Before moving to the concluding section, it remains of interest to look at the impact of small variations of some plasma parameters on the theoretical predictions. As shown in figure 13, the final result of the theoretically predicted value of R/L_{nB} stems from the compensation of contributions of opposite signs. Therefore, it can be expected that relatively small variations of some parameters, for instance the boron logarithmic temperature gradient R/L_{TB} or the boron rotation gradient u'_{Br}, can have a rather large impact on the final predicted value of R/L_{nB}. To this end, in figure 14(a), we show the predicted value of boron in which R/L_{TB} and u'_{Br} are increased by 15%. By this, both outward contributions of thermodiffusion and roto–diffusion are increased. Thereby, the predicted values of R/L_{nB} in the NBI only heated phase (squares) are strongly reduced, and in most cases are very close to zero, and in a few cases even slightly negative, in better agreement with the measured values (we remind also that the uncertainty on the measured values of gradients of the boron density profile is very large, particularly because these profiles are very flat). In figure 14(b) the effect of increasing R/L_{TB} by 30% is shown for the case in which the roto–diffusion contribution is neglected ($D_{UZ} = 0$), which allows the examination of the impact of the temperature gradient alone. This shows that thermo–diffusion alone cannot lead to the prediction of very small values of R/L_{nB}, even by increasing artificially its contribution by 30% (increase of R/L_{Ti} by $\Delta(R/L_{Ti}) \simeq 1.5$, which is actually outside the experimental uncertainty in this parameter). This suggests that roto–diffusion is at least one of the contributions which are predicted theoretically and which have to be included in the modelling to describe the local flattening of the density profiles of impurities like boron

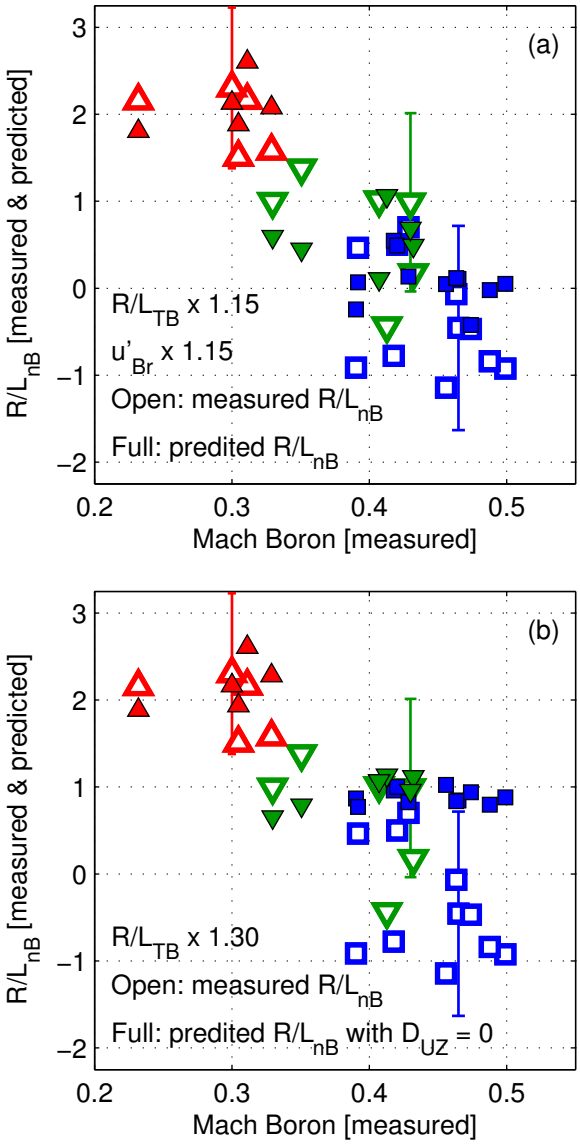

Figure 14. Predicted (full symbols) and measured (open symbols) values of the normalized logarithmic boron density gradient R/L_{nB} as a function of the boron Mach number, for the entire dataset, with NBI heating only (squares), with NBI and low central ECH (triangles pointing down) and with NBI and high central ECH (triangles pointing up), like in figure 12, but (a) with the normalized logarithmic boron temperature gradient R/L_{TB} reduced by 15% and normalized toroidal rotation gradient u'_{Br} increased by the same factor; and (b) with the normalized logarithmic boron temperature gradient R/L_{TB} increased by 15% and excluding the roto–diffusion contribution.

or carbon, which have been observed in experiments.

The tests presented in figure 14 illustrate the sensitivity of the predicted values of R/L_{nB} on the input parameters, particularly for the more strongly rotating phases (with NBI heating only), which also appear to be the most difficult to predict. They also confirm the critical role of the roto–diffusion contribution to account for the almost continuous transition from flat (even hollow in the experiment) to moderately peaked profiles observed in the experiment, when moving from NBI heated only phases, to phases with increasing additional ECH power.

5. Conclusions

Linear and nonlinear gyrokinetic calculations of the local logarithmic electron density gradients R/L_{ne} and linear gyrokinetic calculations of the local logarithmic boron density gradients R/L_{nB}, at mid–radius, have been compared to the experimental measurements obtained in AUG H–mode plasmas at low current with NBI heating and two additional levels of central ECH. The experimental results have been presented, and central electron heating has been shown to increase the peaking of both the electron and the boron density profiles, with the boron profiles remaining always significantly less peaked than the electron profiles. The gyrokinetic modelling turns out to provide predictions which are in good agreement with the experimental measurements for the logarithmic electron density gradient and in reasonable agreement for the boron density gradient. The impact of small modifications of the input parameters for the prediction of R/L_{nB} has been investigated and shown to be significant, which allows us to state that the agreement over the entire dataset of observations, comprising both electron and boron data, is satisfactory.

By this, the theoretical modelling can be used to identify the critical control parameters which govern the observed behaviours of electrons and boron. It has been shown that the increase of the density peaking with increasing additional central ECH power is provided by a combination of effects stemming mainly from the increase of the ratio of the logarithmic electron temperature gradient to the logarithmic ion temperature gradient, and partly also from the increase of the electron to ion temperature ratio, and, less important, from a decrease of collisionality in conditions of dominant ITG instabilities in the phases with NBI heating only and with low ECH power and in conditions with dominant TEM instabilities in the phases with high ECH power. It has been shown that the dependences of R/L_{ne} on all these parameters are captured by the variation of the real frequency of the most unstable mode, which turns out to be a valid ordering parameter for R/L_{ne} over the entire dataset considered. By this application, a confirmation is obtained that the behaviour of the electron density profiles can be interpreted as a macroscopic fingerprint of the microscopic characteristics of the turbulence present in the core of the plasma [1].

The conclusions obtained from the analysis and modelling of the electron density profiles become a constraint in the simultaneous modelling of the boron data, since the the same microinstabilities and turbulence have to explain the observations on both the

transport channels at the same time. Neoclassical boron transport has been found to be almost negligible around mid–radius as compared to the turbulent contributions. In addition, neoclassical transport alone would lead to predictions of boron logarithmic density gradients R/L_{nB} almost one order of magnitude larger than those actually observed. In particular boron is observed to be moderately hollow or flat in conditions of NBI heating only and to increase the peaking with increasing ECH power, up to moderately peaked density profiles. The modelling of boron turbulent transport suggests that the toroidal rotation and its radial gradient are important ingredients to reproduce the observed boron density behaviour. In particular, thermodiffusion alone is not able to describe the variation of the local boron density peaking with increasing ECH power, and is too weak to lead to flat boron density profiles in conditions with NBI heating only. The inclusion of roto–diffusion allows the observed increase of R/L_{nB} from NBI only phases to strong ECH phases to be reproduced by the modelling, but it turns out not to be large enough to lead to the prediction of locally hollow density profiles in the phases with NBI only. In phases with high ECH power, roto–diffusion becomes negligible, due to the slowing down of the plasma toroidal rotation velocity, while the inward contributions of the pure convection and of the thermodiffusion produced by dominant TEM instabilities allow the simulations to predict the experimental values with high accuracy. By these results, an ingredient in the modelling of impurity transport is pointed out, namely the toroidal rotation velocity and its radial gradient, which can become important under some conditions. This has been largely neglected so far in the modelling of experiments of impurity transport, but is likely to be at least one of the missing ingredients required to explain the rather generic observations of flat or even hollow density profiles of relatively light impurities like carbon in typical, NBI heated, H–mode plasmas.

With the present results, we would also like to motivate further experimental and theoretical studies exploring the impact of rotation on impurity transport, when possible comparing light with heavy impurities. In particular, from the theoretical side, the inclusion of centrifugal effects, which have been neglected in the present study, but which might not be completely negligible even for the modelling of boron, appears to become mandatory for heavier impurities, in experimental conditions like those considered in this work. From the experimental standpoint, the present results suggest that flat or even slightly hollow density profiles of light impurities can be obtained in the confinement region around mid–radius provided that the toroidal rotation velocity and its radial gradient are sufficiently large. This indication certainly deserves further experimental investigations.

Acknowledgments

One of the Authors (C.A.) would like to thank Y. Camenen, F. Casson and A.G. Peeters for very fruitful discussions. The Authors are grateful to J. Candy and R. E. Waltz for providing the gyrokinetic code GYRO as well as to W. Dorland and M. Kotschenreuther for providing the gyrokinetic code GS2. Simulations were performed on the parallel

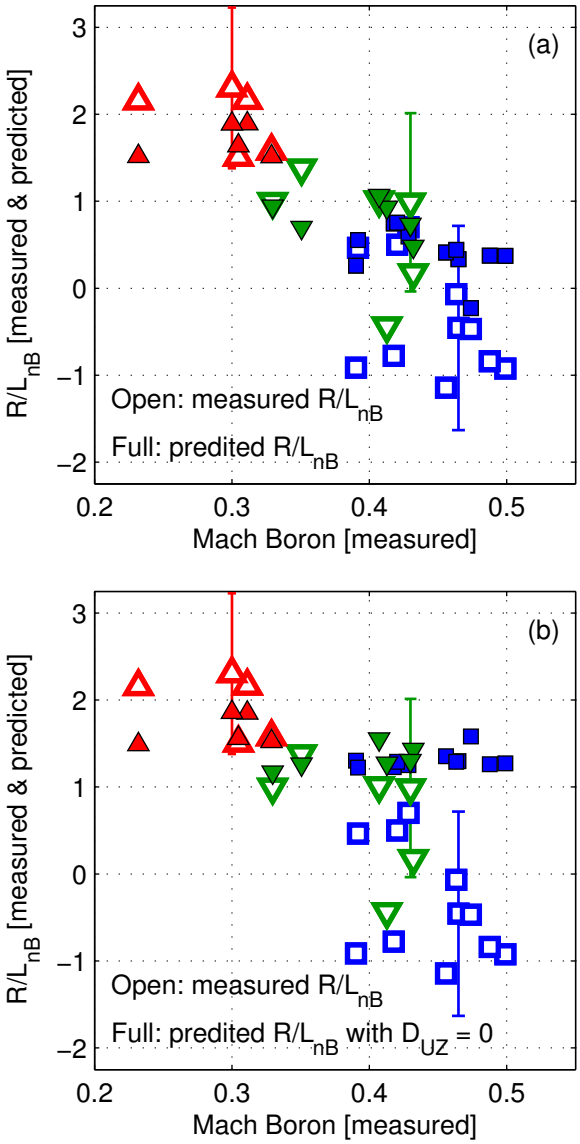

Figure 15. Predicted (full symbols) and measured (open symbols) values of the normalized logarithmic boron density gradient R/L_{nB} as a function of the boron Mach number, for the entire dataset, with NBI heating only (squares), with NBI and low central ECH (triangles pointing down) and with NBI and high central ECH (triangles pointing up), but this time with GS2 calculations of boron transport performed using the theoretically predicted values of R/L_{ne} as inputs, shown in figure (7), and not the experimentally measured values, which were used for the results presented in figure 12. Analogously to figure 12, in (a) all of the boron transport terms in Eq. (6) are included, in (b) the effect of roto–diffusion is excluded for comparison, that is with $D_{UZ} = 0$ in Eq. (6).

server Power-6 (Vip) of the IPP-MPG Rechenzentrum Garching, Germany and on the server High Parallel Computing for Fusion (HPC-FF) at the Forschungzentrum Juelich, Germany.

Appendix, Modelling of R/L_{nB} using predicted R/L_{ne} as an input

As anticipated, here we show the results obtained by using the theoretically predicted values of the logarithmic electron density gradient R/L_{ne} (and not those experimentally measured) as inputs to the gyrokinetic calculations of boron transport. The results are presented in figure 15(a), and show predicted values of the logarithmic boron density gradient R/L_{nB} which are very close to those obtained when experimentally measured values of R/L_{ne} are considered as inputs, which were shown in figure 12(a). This was to be expected, since the predicted values of R/L_{ne} are sufficiently close to the measured values. Analogously to figure 12(b), in figure 15(b), the same comparison is illustrated, but with the contribution from roto–diffusion removed. This plot confirms the important role of roto–diffusion in predicting the experimentally observed trend of increasing R/L_{nB} with increasing central ECH power.

[1] Angioni C., Fable E., Greenwald M., Takenaga H., Weisen H. 2009 *Plasma Phys. Control. Fusion* **51** 124017.
[2] Gilgenbach R. M. *et al* 1980 *Phys. Rev. Lett.* **44** 647.
[3] Riviere A. C. 1986 *Nucl. Fusion* **28** 1995.
[4] TFR Group 1988 *Nucl. Fusion* **28** 1995.
[5] Weisen H., Furno I., Alberti S. *et al* 2002 *Nucl. Fusion* **42** 136.
[6] Stober J., Dux R., Gruber O. *et al* 2003 *Nucl. Fusion* **43** 1265.
[7] Angioni C., Peeters A. G., Garbet X. *et al* 2004 *Nucl. Fusion* **44** 827.
[8] Hoang G. T., Bourdelle C., Garbet X. *et al* 2004 *Phys. Rev. Lett.* **93** 135003.
[9] Weisen H., Zabolotsky A., Garbet X. *et al* 2004 *Plasma Phys. Control. Fusion* **46** 751.
[10] Angioni C., Peeters A.G., Ryter F., Jenko F., Conway G. D., Dannert T., Fahrbach U.H., Reich M., Suttrop W., Fattorini L. 2005 *Phys. Plasmas* **12** 040701.
[11] Zabolotsky A., Weisen H. and TCV Team 2006 *Plasma Phys. Control. Fusion* **48** 369.
[12] Romanelli M., Hoang G. T., Bourdelle C. *et al* 2007 *Plasma Phys. Control. Fusion* **49** 935.
[13] Razumova K. A., Andreev V. F., Dnestrovskij A. Yu. *et al* 2008 *Plasma Phys. Control. Fusion* **50** 105004.
[14] Jacchia A. *et al*, *Density response to modulated EC Heating in FTU Tokamak*, 37th EPS Conference on Plasma Physics 2010, Dublin, P1.1045 and http://ocs.ciemat.es/EPS2010PAP/pdf/P1.1045.pdf
[15] Dux R., Neu R., Peeters A.G., Pereverzev G., Mück A., Ryter F., Stober J., Plasma Phys. Control. Fusion **45**, 1815 (2003).
[16] Scavino E., Bakos J., Weisen H. 2004 *Plasma Phys. Control. Fusion* **46** 857.
[17] Puiatti M.E., Valisa M., Angioni C., Garzotti L., Mantica P., Mattioli M., Carraro L., Coffey I., Sozzi C. 2006 *Phys. Plasmas* **13** 042501.
[18] Angioni C., Dux R., Fable E. *et al* 2007 *Plasma Phys. Control. Fusion* **49** 2027.
[19] Villegas D., Guirlet R., Bourdelle C., Hoang G.T., Garbet X. and Sabot R. 2010 *Phys. Rev. Lett.* **105** 035002.
[20] Angioni C, Peeters A G, Pereverzev G V *et al* 2003 Phys. Plasmas **10** 3225.
[21] Garbet X, Garzotti L, Mantica P *et al* 2003 *Phys. Rev. Lett.* **91** 035001.
[22] A. Kallenbach, R. Dux, M. Mayer, R. Neu, T. Pütterich *et al* 2009 *Nucl. Fusion* **49** 045007.
[23] McDermott R.M. *et al*, *Core Toroidal Rotation Changes Observed with ECRH Power in NBI Heated H-modes on ADSEX Upgrade*, 37th EPS Conference on Plasma Physics 2010, Dublin, P1.1062 and http://ocs.ciemat.es/EPS2010PAP/pdf/P1.1062.pdf
[24] McDermott R.M. *et al* 2011 *Plasma Phys. Control. Fusion* **53** 035007
[25] Fischer R., Fuchs C.J., Kurzan B., Suttrop W., Wolfrum E. and the ASDEX Upgrade Team 2010

Fusion Science and Technology **58** 675.
[26] Manini A., Ryter F., Angioni C. *et al* 2004 *Plasma Phys. Control. Fusion* **46** 1723.
[27] Manini A., Angioni C., Peeters A.G. *et al* 2006 *Nucl. Fusion* **46** 1047.
[28] Weisen H., Zabolotsky A., Angioni C. *et al.* 2005 *Nucl. Fusion* **45** L1.
[29] C Giroud in Fusion Energy 2006 (Proc. 21st Int. Conf. Chengdu, 2006) (Vienna: IAEA) CD-ROM file EX/8–3 and http://www-naweb.iaea.org/napc/physics/FEC/FEC2006/html/index.htm
[30] Angioni C., Peeters A.G., Pereverzev G.V., Ryter F., Tardini G., and ASDEX Upgrade Team 2003 *Phys. Rev. Lett.* **90** 205003.
[31] Weisen H., Zabolotsky A., Maslov M., Beurskens M., Giroud C., Mazon D. 2006 *Plasma Phys. Control. Fusion* **48** A457.
[32] Greenwald M., Angioni C., Hughes J. W., Terry J. and Weisen H. 2007 *Nucl. Fusion* **47** L26.
[33] Takenaga H., Tanaka K., Muraoka K. *et al* 2008 *Nucl. Fusion* **48** 075004.
[34] Angioni C., Weisen H., Kardaun O.J.W.F. *et al.* 2007 *Nucl. Fusion* **47** 1326.
[35] Maslov M., Angioni C. and Weisen H. 2009 *Nucl. Fusion* **49** 075037.
[36] ITER Physics Basis Expert Groups on Confinement and Transport and Confinement Modelling and Database, ITER Physics Basis Editors 1999 *Nucl. Fusion* **39** 2175.
[37] Kotschenreuther M., Rewoldt G., and Tang W.M. 1995 *Comput. Phys. Commun.* **88** 128.
[38] Dorland W., Jenko F., Kotschenreuther M., Rogers B.N. 2000 *Phys. Rev. Lett.* **85** 5579.
[39] Candy J. and Waltz R.E. 2003 *J. Comput. Phys.* **186** 545.
[40] Candy J. and Waltz R.E. 2003 *Phys. Rev. Lett.* **91** 045001.
[41] Nevins W.M., Parker S.E. and Chen Y., Candy J., Dimits A., Dorland W., Hammett G.W., Jenko F. 2007 *Phys. Plasmas* **14** 084501.
[42] Angioni C. and Peeters A.G 2008 *Phys. Plasmas* **15** 052307.
[43] Miller R.L., Chu M.S., J.M. Greene, Lin–Liu Y.R., and Waltz R.E. 1998 *Phys. Plasmas* **5** 973.
[44] Pankin A. *et al* 2004 *Comput. Phys. Commun.* **159** 157.
[45] Bourdelle C., Garbet X., Imbeaux F. *et al* 2007 *Phys. Plasmas* **14** 112501.
[46] Zabolotsky A., Weisen H., Karpushov A. *et al* 2006 *Nucl. Fusion* **46** 594.
[47] Poli E., Peeters A.G. and Pereverzev G.V. 2001 *Comp. Phys. Commun.* **136** 90.
[48] Pereverzev G.V. and Yushmanov P.N. 2002 *"ASTRA automated system for transport analysis in a tokamak"*, Report IPP5/98, Max–Planck–Institut für Plasmaphysik, Garching.
[49] Houlberg W.A., Shaing K.C., Hirshman S.P., Zarnstorff M.C. 1997 *Phys. Plasmas* **4** 3230.
[50] Angioni C. and Sauter O. 2000 *Phys. Plasmas* **7** 1224.
[51] Angioni C., Candy J., Fable E., Maslov M., Waltz R.E., Weisen H. 2009 *Phys. Plasmas* **16** 060702.
[52] Waltz R. E., Casati A., Staebler G. 2009 *Phys. Plasmas* **16** 072303.
[53] Hein T., Angioni C., Fable E., Candy J. 2010 *Phys. Plasmas* **17** 102309.
[54] Ernst D. R., Bonoli P. T., Catto P. J. *et al* 2004 *Phys. Plasmas* **11** 2637.
[55] Fable E., Angioni C., Sauter O. 2010 *Plasma Phys. Control. Fusion* **52** 015007.
[56] Fable E., Angioni C. and Sauter O. 2008 *Plasma Phys. Control. Fusion* **50** 115005.
[57] Estrada-Mila C., Candy J., Waltz R. E. 2006 *Phys Plasmas* **13** 074505.
[58] Angioni C., Peeters A.G., Pereverzev G.V., Bottino A., Candy J., Dux R., Fable E., Hein T. and Waltz R.E. 2009 *Nucl. Fusion* **49** 055013.
[59] Camenen Y., Peeters A.G., Angioni C. *et al* 2009 *Phys. Plasmas* **16** 012503.
[60] Frojdh M., Liljestrom, Nordman H. 1992 Nucl. Fusion **32** 419.
[61] Garbet X., Dubuit N., Asp E., Sarazin Y, Bourdelle C., Ghendrih P., Hoang G.T. 2005 *Phys. Plasmas* **12** 082511.
[62] Angioni C. and Peeters A.G. 2006 *Phys. Rev. Lett.* **96** 095003.
[63] Dubuit N., Garbet X., Parisot T., Guirlet R., and Bourdelle C. 2007 *Phys. Plasmas* **14** 042301.
[64] Fülöp T., Braun S., and Pusztai 2010 *Phys. Plasmas* **17** 062501.
[65] Kluy N., Angioni C., Camenen Y., Peeters A.G. 2009 *Phys. Plasmas* **16** 122302.
[66] Peeters A.G., Strintzi D., Camenen Y. *et al* 2009 *Phys. Plasmas* **16** 042310.
[67] Peeters A.G., Angioni C. Strintzi D. 2007 *Phys. Rev. Lett.* **98** 265003.
[68] Peeters A.G., Camenen Y., Casson F.J., Hornsby W.A., Snodin A.P., Strintzi D. and Szepesi G.

2009 *Comp. Phys. Comm.* **180** 2650.
[69] Casson F., Peeters A.G., Angioni C. *et al* 2010 *Phys. Plasmas* **17** 102305.